3D digital holographic interferometry and spectral optical coherence tomography for the measurement of strain in metallic objects and phase in biological tissues

Presented by

M.C. Manuel Humberto De la Torre Ibarra

Thesis submitted as partial fulfillment of the requirements for the award of Doctor of Sciences from Centro de Investigaciones en Óptica A.C.

April 2006

Dedicatory

To Mónica, Valeria and Manuel Jr.

Thank you for all your patient

Acknowledgments

It has been a very long journey since I joined to the CIO in 2000 and I would like to express my gratitude to my supervisor, Dr. Fernando Mendoza Santoyo, whose expertise, support and patience, added considerably to my professional experience. I appreciate his vast knowledge and skills in many areas of optics. I really appreciate his effort and support to help me to find a pre doctoral stay at Loughborough University. I would like to thank Dr. Jonathan M. Huntley and Dr. Pablo D. Ruiz for their time and patient during those months where I learned a lot. Finally, I would like to thank Dr. Carlos Perez Lopez, Dr. Ramón Rodríguez Vera and Bernardino Barrientos Garcia from the metrology group for taking time out from his busy schedule to serve as my internal readers.

I must acknowledge Dr. Francisco Cuevas, Dr. Manuel Servín, Dr. Sergio Calixto, Dr. Evguenii Kourmychev, Dr. Daniel Malacara, Dr. Oracio Barbosa, Dr. Bernardo Mendoza, Dr. Francisco Marín, Dra. Cristina Solano, Dr. Ricardo Flores and Dr. Rafael Luna who truly made a difference during my studies with their motivation and encouragement.

I would like to thanks to all CIO personnel who help me at any time and always they try to give me their best. And special mention to Rodolfo Zamarripa, Ricardo Valdivia, Guillermina Muñiz, Angeles Sanchez and the entire academic department who help me at any time and their assistance help me along the way.

I would also like to thank my friends in the CIO and Loughborough University, particularly my generation classmates, for their philosophical debates, exchanges of knowledge, and venting of frustration during my PhD. program, which help me to enrich the experience

I recognize that this research would not have been possible without the financial assistance of the CONACYT and the University of Loughborough and I express my gratitude to those agencies.

Content

Abstract

The present work is devoted to two optical non destructive tests as digital holographic interferometry and spectral optical coherence tomography. Both techniques were successfully applied to detect strain and phase in metallic and organic samples respectively. The mainly differences between these two techniques is their penetration factor. Three-dimensional digital holography was applied for the detection of surface displacements in metallic objects. Modeling displacements with this technique make it possible to generate a surface strain map over the whole field of view of the system. In this particular case, the optical set up uses illuminating beams to irradiate the object from three different directions resulting that all three x, y and z displacement components can be independently analyzed and used to find the strain gradients on the surface of the sample. Furthermore, separation of the surface strain gradients as function of *x* and *y* was achieved with the same optical system. Results show the conversion of the complete surface displacement field into a surface strain field with no extra hardware. The second non destructive test is the spectral optical coherence tomography used to measure sub-surface optical phase within a transparent (pig cornea) media. The system provides displacement maps within a 2-D slice extending into the sample. The proof of principle of the method was done with low cost components in a system with no moving parts set in a novel data processing for this kind of information. The method was used to explore an organic sample in order to get optical phase information within the sample. Results showed a system high sensitivity and its viability for sub-surface inspection.

1. Introduction

Optics has been widely used in different fields to obtain information otherwise difficult to obtain with mechanical systems. Specifically, the optical non invasive methods have the advantage to measure the object with minimum perturbations. Present work applies two different optical techniques with a common end which is the displacement measurement even in different samples. Displacement and strain measurements have been studied in optics with techniques like, fringe projection, electronic speckle pattern interferometry (ESPI), digital holographic interferometry (DHI) and moiré [1-18]. Displacements are equally widely studied in mechanical literature with different objects and considerations [19-24]. Displacements can be read as a response of the object structure under a deformation (internal or external). This deformation has to be controlled in order to reproduce its impact in the sample. Later, will give an idea about the mechanical properties of the object under study and sometimes is possible to do some estimations of it if they are modeled.

First study presented in this work involves DHI applied to metallic objects. Metal properties are well known in most common cases and there is extensive literature about them [25-27]. DHI is a remote technique which allows having full field inspection with high sensitivity. Also, this method is similar to ESPI but the phase recover is one major difference between them [28]. Both techniques have similar set up configurations where scattering coming from the object under study is combined with a reference beam. This

interference pattern is related to the deformation applied to the object. With these interferometric techniques it is possible to have a system which is going to be sensitive to just few microns (~10^{-6}). There is a common tool used in these techniques: –a quasi monochromatic source of illumination–, a laser, has been used in most of the interferometric systems of digital holographic interferometry [29, 30] or electronic speckle pattern interferometry [31, 32]. Scattering coming from the object in an interferometric system gives the behavior of the object according with its deformation. Two-exposure time method is used in both cases to obtain the change of the object in two different states. Development and increasing technology in laser allows more complex and advanced systems dealing in dynamic or static events.

Using three-dimensional digital holographic is possible to isolate each displacement magnitude x, y and z. This particular characteristic is useful to processes this data in order to have a strain gradient map. Strain fields represent changes of points over the surface of the object which is directly related with the kind of object and deformation applied. A mathematical model is introduced describing the relation between DHI data and the strain gradient theory. Also, conditions required to apply it are well described [20, 33]. Normal strain presented with DHI gives the advantage to observe a full field strain map and a more complex strain distribution. Finally, it is very important considering that results obtained show not just magnitude from strain gradients, also, they show direction where strain is increasing or decreasing [34]. Under this method a

good response is achieved in different deformations with metallic objects presenting different stiffness among them.

The second part of this work relates to a technique called spectral optical coherence tomography (SOCT) which is so called a penetration technique. Optical Tomography generates two dimensional slices coming from a three dimensional object. Most of its applications are reserved to medical applications moving last decade to other fields of research [35, 36]. Optical coherence tomography (OCT) is a non destructive test that can be used in time, spectral and quantum domain [37]. A SOCT system is described and validated with a two beam interferometer mounted in the same system in order to perform a measurement of displacement in a media. With the validation process is possible to have confidence in posterior measurements in a scattering media. System parameters are described and mathematical assumptions also. As scattering media an organic cornea is used where phase maps are well detected with a depth ~3 mm. Penetration is possible thanks to a different source of illumination which is a broad band source. Results obtained show high sensitivity with this technique even when low scattering is present in the samples.

This new form to process DHI and OCT data results makes the present work a relevant contribution to non destructive tests where a high information quantity data is desired in future applications.

2. Concepts and mathematical model

This chapter is divided principally in two sections; the first one describes the DHI method and shows how this technique can be used to determine surface strain gradients. The second section is devoted to SOCT and its mathematical description and how it is possible to determine displacements and phase information in organic samples. Each section is subdivided in order to have a clearer explanation of the concepts. Very basic concepts are omitted for simplicity; this research presents applications of non destructive tests already known but introducing a new way as this information is processed.

2.1. Digital Holographic Interferometry

The variable of interest to be found is the phase or the path length difference between the reference and object light paths that takes place when the object undergoes a deformation. The amplitude may be measured straightforwardly by simply counting the number of fringes and multiplying it by a constant that depends on the wavelength of the laser light used. When using DHI to study object displacements, the CCD camera sensor is only able to detect an amount of light directly proportional to the wave field intensity produced by the overlapping or interference between the object and reference beams, viz.,

$$I(x,y) = I_R + I_O + 2\sqrt{I_R I_O}\cos(j + y) \tag{2.1}$$

where I_O and I_R are the mean intensities due to object and reference beams, j denotes the randomness of the speckle field coming from the object, and the additional phase difference y represents the surface deformation/displacement. If the application in hand involves only static displacements j and y do not vary with time. The usual procedure in static or dynamic events is subtraction between two object-reference beam images at two different object positions is performed. With DHI and SOCT the images have to be PC hardware captured. The data acquired is processed with a Fourier algorithm [38, 39] in order to obtain a relative wrapped phase map. Figure 2.1 shows general stages for DHI.

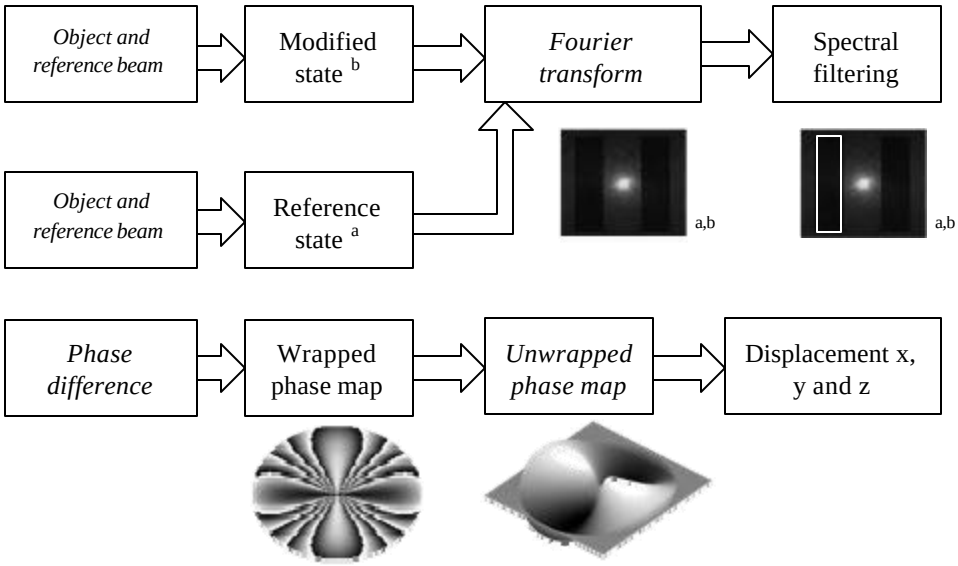

Figure 2.1. Different stages in DHI. This process is repeated three further times with every illumination position (3D DHI). Process involves these three unwrapped phase maps to obtain 3D (x,y,z) displacements.

The wrapped phase map is processed with recurrent phase unwrapping software (Phase Vision Ltd. Pv_spua2), a process that gives the whole field displacement phase map that is ultimately processed in the usual manner. Once the displacement along x, y and z is obtained an algorithm is applied in order to change a into strain gradient maps, as explained in the next section.

2.1.1. Mathematical model of strain for metallic objects

For metallic objects displacement is a geometric quantity independent of the object shape. A displacement may be manly considered as the sum of two components: the displacement of the body as a whole, also known as rigid body motion, and the relation of movement between one point in or on the body with respect to another, called real body displacement [20, 21]. The relationship between the former and the object stress/strain can be expressed through Hooke´s law,

$$\sigma = E\,\varepsilon \tag{2.2}$$

where σ is the stress, ε is the strain and E the elasticity modulus. Equation 2.2 involves in a direct proportionality the strain and the stress, a feature that applies for rigid body displacements. For instance, a force acting along the y-axis will cause strain in the x and z directions. At this point the concept of normal strain is introduced as that related to

both the real body displacement theory and the rigid body motion, so that equation (2.2) takes the form, for the y-axis force,

$$e_{yy} = \sigma yy / E \tag{2.3}$$

$$e_{xx} = e_{zz} = - (? \sigma yy / E) \tag{2.4}$$

where e_{xx}, e_{yy}, e_{zz} represent the strain in orthogonal directions, and ? is the Poisson's ratio. When a force system acts upon the object a displacement along the x, y and z axes is represented by u, v, and w respectively. Given known initial conditions for the object its displacement components u, v, w can each be expressed by means of a Taylor series expansion with respect to x, y, and z, giving as a result the normal strain orthogonal gradients [20, 21]:

$$e_{xx} = \sqrt{1 + 2\frac{\partial u}{\partial x} + \left(\frac{\partial u}{\partial x}\right)^2 + \left(\frac{\partial v}{\partial x}\right)^2 + \left(\frac{\partial w}{\partial x}\right)^2} - 1 \tag{2.5}$$

$$e_{yy} = \sqrt{1 + 2\frac{\partial v}{\partial y} + \left(\frac{\partial v}{\partial y}\right)^2 + \left(\frac{\partial w}{\partial y}\right)^2 + \left(\frac{\partial u}{\partial y}\right)^2} - 1 \tag{2.6}$$

$$e_{zz} = \sqrt{1 + 2\frac{\partial w}{\partial z} + \left(\frac{\partial w}{\partial z}\right)^2 + \left(\frac{\partial u}{\partial z}\right)^2 + \left(\frac{\partial v}{\partial z}\right)^2} - 1 \tag{2.7}$$

where e_{xx}, e_{yy} and e_{zz} are the normal strain gradients along x, y and z respectively. Now, the rate of change ¶u/¶x, ¶v/¶y and ¶w/¶z represent displacement variations parallel to x, y and z, respectively. These equations are shown unexpanded with the condition for the applied deformation being introduced. The deformation must be small so that it will not change the mechanical properties of the object, e.g., planes will remain planes and straight lines will remain straight lines. The z gradient cannot be determined with the coplanar set up (see figure 2.2) because the axis of observation is along the z direction. However, it is possible to find the x and y gradients and equations 2.5 and 2.6 can be reduced to,

$$e_{xx} = \frac{\partial u}{\partial x} \tag{2.8}$$

$$e_{yy} = \frac{\partial v}{\partial y} \tag{2.9}$$

respectively. If the conditions mentioned above are met, these relations make it possible to convert a displacement field into a strain field. Where the displacements along x, y and z axis are represented by u, v and w respectively. These equations were determined considering the engineering strain definitions,

$$e_{xx} = \frac{\Delta x' - \Delta x}{\Delta x} \tag{2.10}$$

$$e_{yy} = \frac{\Delta y' - \Delta y}{\Delta y} \tag{2.11}$$

$$e_{zz} = \frac{\Delta z' - \Delta z}{\Delta z} \tag{2.12}$$

where *Dx*, *Dy* and *Dz* are the original object dimensions along the corresponding x, y and z axes, and *Dx'*, *Dy'* and *Dz'* represent the resultant dimensions after deformation. Equations 2.10, 2.11 and 2.12, are the strain gradients along *x*, *y* and *z* respectively and represent the contribution in the corresponding axis. In order to have the whole object strain response due to the deformation, the dependence with the rest of the axes must be introduced. This means that the gradient in x depends on *u*, *v* and *w* displacements. The same applies for the y and z gradients, as seen in equations 2.5, 2.6 and 2.7. It is possible to rewrite these equations if the optical coplanar set up is used. The dependence is thus reduced to the xy plane with the z gradient becoming an out-of-plane magnitude (e_{zz} constant). The strain gradients e_{xx} and e_{yy} may hence be expressed as a function of *x* and *y*,

$$e_x(x, y) = \frac{\partial f}{\partial x \partial y} \tag{2.13}$$

$$e_y(x, y) = \frac{\partial f'}{\partial y \partial x} \tag{2.14}$$

where *f* and *f'* denote the x and y strain gradient with dependence in *x* and *y*, respectively. From equations 2.13 and 2.14, it is possible to determine the dependent

gradient as function of x and y separately for each strain gradient. To obtain these dependent gradients, a partial derivation with respect to x and y is needed, giving

$$e_x(x) = \frac{\partial f}{\partial x} \tag{2.15}$$

$$e_x(y) = \frac{\partial f}{\partial y} \tag{2.16}$$

$$e_y(x) = \frac{\partial f'}{\partial x} \tag{2.17}$$

$$e_y(y) = \frac{\partial f'}{\partial y} \tag{2.18}$$

Equations 2.15 and 2.16 are the mathematical derivation from the f gradient with respect to x and y respectively. Considering that x and y are independent of each other it is possible to construct the dependent gradient maps for each one. Equations 2.17 and 2.18 are used in a similar way to obtain the x and y dependence of the f' gradient. Dependent gradients are the variation of the surface strain observed with just one variable at the time, and they change depending on the normal strain gradient they are derivate from. Thus, the dependent gradient maps show the maximum variation in strain gradient separated from its two variables. With all this it is possible to have with the same optical set up a system capable to detect six strain maps with the possibility to extend it at three more of shear strain.

2.1.2. Joining DHI data with surface strain model

Join DHI displacement data with strain model requires extra data processing considering that phase information is relative and there are three different sources of illumination. A DHI technique involves a matrix sensitivity vector described in equation 2.19.

$$\frac{l}{2p}\begin{pmatrix}\Delta y_1\\ \Delta y_2\\ \Delta y_3\end{pmatrix}=\begin{pmatrix}k_{1x} & k_{1y} & k_{1z}\\ k_{2x} & k_{2y} & k_{2z}\\ k_{3x} & k_{3y} & k_{3z}\end{pmatrix}\begin{pmatrix}u\\ v\\ w\end{pmatrix} \tag{2.19}$$

Where $k_{n\,x,y,z}$ is the sensitivity vector (see appendix A) and $??_n$ is the resultant phase, from every illuminating position. As $??_n$ and $k_{n\,x,y,z}$ are known from the experimental set up, equation 2.19 may be solved for each object displacement component *u*, *v*, and *w*. This particular characteristic makes possible to have an approximation with equations 2.5 trough 2.7. But, these three last equations have axis combinations with the whole displacements as the strain tensor shows.

$$\begin{pmatrix}\frac{\partial u}{\partial x} & \frac{\partial u}{\partial y} & \frac{\partial u}{\partial z}\\ \frac{\partial v}{\partial x} & \frac{\partial v}{\partial y} & \frac{\partial v}{\partial z}\\ \frac{\partial w}{\partial x} & \frac{\partial w}{\partial y} & \frac{\partial w}{\partial z}\end{pmatrix}=\begin{pmatrix}e_{xx} & g_{xy} & g_{xz}\\ g_{yx} & e_{yy} & g_{yz}\\ g_{zx} & g_{zy} & e_{zz}\end{pmatrix} \tag{2.20}$$

$g_{n\,x,y,z}$ are shear strain components in different combinations, but in this case strain tensor is reduced. Shear strain xy and yx are omitted to processes them under

consideration that major strain contribution is present in normal strain x and y. However, a system able to achieve all components will require extra hardware set up and more than one detector. For this reason a coplanar system is required to have same axis components observed by the system under a deformation in samples (see figure 2.2).

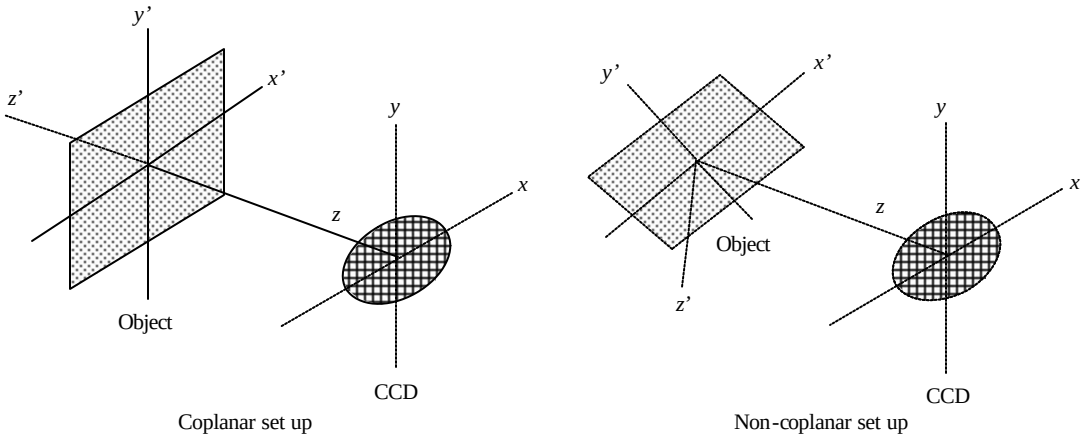

Figure 2.2. Object and CCD sensor orientation in an aligned and not aligned set up. In a coplanar system *z*-axis is the same for object and CCD sensor.

Considering reduced equations 2.8 and 2.9, a relation can be performed with strain gradients and displacement magnitudes. A derivative algorithm is performed to take displacement magnitudes to transform them as strain gradients. This algorithm creates combinations with displacement magnitudes to obtain gradient magnitudes at each axis. Later makes possible to have a strain gradient with independent contributions with no extra hardware. These strain gradients can be shown as magnitude maps or three dimensional sparse vector maps. First ones can show color bars depending of strain magnitude, but, second ones take advantages for full field information and consider pixels as independent elements and show magnitude and direction of strain gradients.

Even when this sparse vector map looks in two dimension three dimensional information is already added with the origin and the end of these vectors. Vector size is directly related with the strain present at that single point. With coplanar set up high sensitivity is obtained with z gradient detected as an out of plane magnitude used to generate direction where the micro strain is growing.

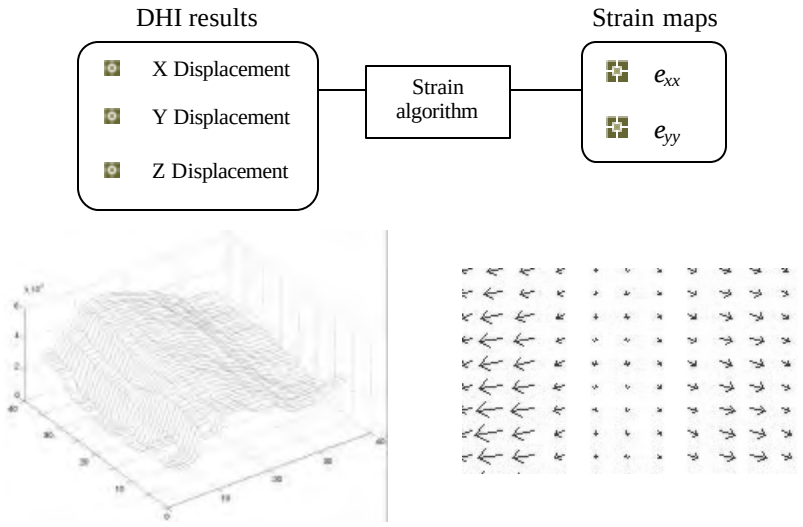

Figure 2.3. Strain maps generation coming from independent displacement fields. Direction view is possible thanks to out of plane contribution in z-axis.

At this point normal strain gradients are already obtained with DHI information. A further analysis involves each strain gradient map; as was described previously they have derivative information for each axis. This one can be processed to separate it as a dependent gradient for each axis component. Equations 2.13 and 2.14 derivate gradients with each variable x and y at the time generating four new gradients. These dependent gradients (equations 2.15 trough 2.18) have a strong contribution for each axis at the

time. One advantage of this is to have the three dimensional contribution already added before with z magnitude. These maps have more information for every axis because they are taken for independent gradients in *x* or *y*.

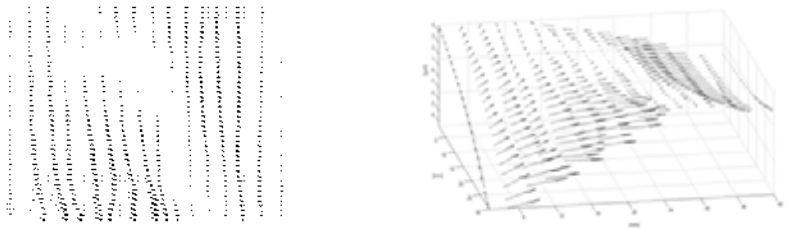

Figure 2.4. Enhancement in dependent gradient maps respect to normal gradient maps.

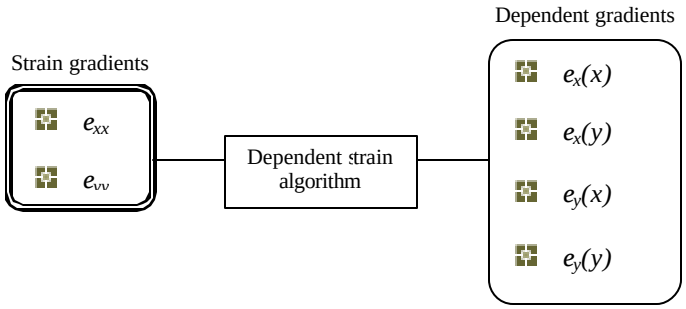

Figure 2.5. Gradient map separation in dependent gradient maps. Posterior algorithm is performed to derivative in axes components.

2.2. Tomographic techniques

The main objective of Tomographic techniques is to inspect a three dimensional media generating 2D image slices of it. These tomographic techniques are developed with magnetic, ultrasonic and optical systems. Optical tomography involves optical diffraction tomography (ODT) and diffuse optical tomography (DOT). DOT uses diffusely propagation of photons trough a media to recover internal information of it. ODT uses scattered light coming from the media and obtains images by Fourier diffraction projection theorem. Low coherence interferometry (LCI) and optical coherence tomography (OCT) are subdivisions of ODT. LCI is applied in time domain while OCT can be applied in time or spectral domain and use ballistic and near ballistic photons to get sample information. Time domain OCT scans a line over the sample meaning that these systems have moving parts. But nowadays has one of the biggest advances respect to spectral domain. Spectral domain OCT (SOCT) normally is one shot system with no moving parts and the whole line is inspected at the time and has been studied for the last decade [40-51]. SOCT system normally uses Fourier transform to recover depth information of the sample. This is an advantage because many algorithms are already available. Some recent reports emphasize SOCT high sensitivity to recover depth information [52]. Even thought most of actual applications are developed in time domain what implies a great challenge for spectral systems.

2.2.1. Spectral Optical Coherence Tomography

SOCT can be considered as a parallel form of wavelength scanning interferometry (WSI) where a tunable laser is used to generate a broad band source [53, 54]. Scanning time generates a model based in time (t) as variable. However in SOCT set up, source is already a broadband which generates a model based in wavelength (l) as variable (see figure 2.6).

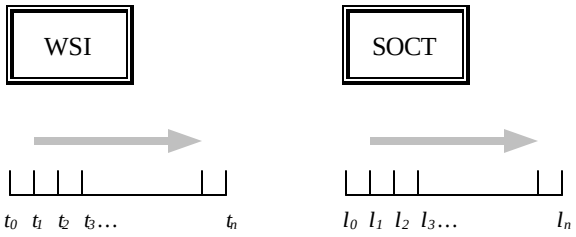

Figure 2.6. Variable difference between wavelength scanning interferometry and spectral optical coherence tomography set ups

Broadband source illuminates a narrow 'sheet' (as opposed to extended volume for WSI) extending into the sample surface and a diffraction grating separates the different wavelength components of both the back-scattered light and a reference beam along the perpendicular direction (see Figure 2.7). A typical interference pattern from a simple sample, consisting of a plane mirror, is shown in figure 2.8. Each column represents the interference pattern for the illuminated stripe on the mirror at a given wavelength. The direct equivalence between the space dimension in this technique, and time in WSI, means that the equations (basic parameters) derived in [54] can be applied directly here.

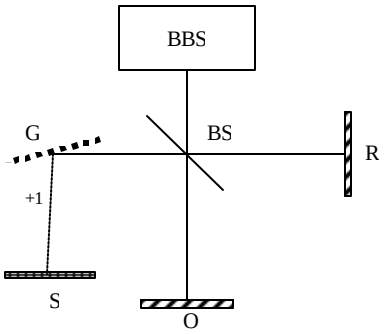

Figure 2. 7 Typical SOCT system consisting of a broad band source (BBS), a mirror as object (O), reference mirror (R), beam splitter (BS), diffraction grating in first diffraction order (G) and sensor (S). Light coming out from BBS is a sheet perpendicular to the paper.

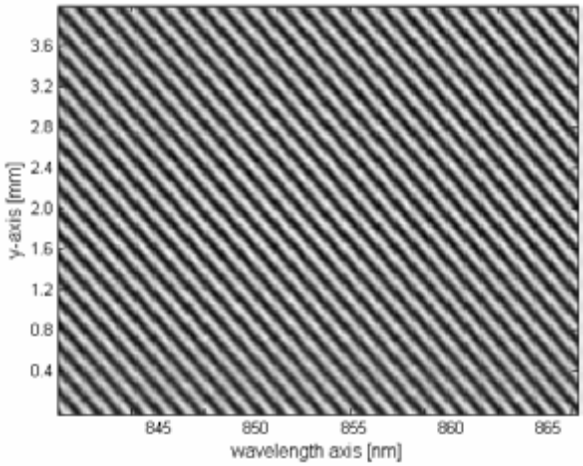

Figure 2.8. Typical SOCT interference pattern with sample consisting of a single plane mirror.

A broadband source emits light centered at l_c with a bandwidth Dl distributed along the l-axis of the camera. Assuming that all wavelengths in Dl are linearly distributed along the l-axis, the wavelength increment between successive pixels is $dl = Dl/N$, where N represents the number of pixels along the l-axis. The maximum optical path difference

between the scattering layer and reference mirror for a SOCT system (depth range) is fixed by the Nyquist frequency for the fringes along the l-axis as

$$\Lambda z = \frac{N l_c^2}{4\Delta l} \tag{2.21}$$

The effective coherence length l_c for the light source is dependent on the pixel fill factor along the l-axis. However, even when the fill factor is 100%, the first zero in the fringe visibility occurs when the optical path difference between the deepest scattering layer and reference mirror is Dz. Therefore, provided the product between the maximum sample depth and its refractive index does not exceed the value given by equation 2.21, the coherence length of the light source is not a limitation of the technique.

Separation of scattering points along the z axis is achieved by Fourier transformation along the l-axis [55]. A deeper point in the object will have a higher intensity modulation frequency associated with it and vice versa. Frequency can be written in several ways; here we express it in terms of l as shown in equation 2.22:

$$f_j = \frac{2}{l_c^2} z_j \tag{2.22}$$

where z_j is the optical depth of the jth scattering layer (i.e., one half of the round trip optical path difference between the reference and scattering surfaces), and the units of f_j are cycles per unit length. This frequency can alternatively be written in units of cycles pixel^{-1} as shown in equation 2.23.

$$f_j^{'} = \frac{2\Delta l}{N l_c^2} z_j \tag{2.23}$$

The depth resolution of the system is the minimum axial distance between two points inside the medium that can be resolved independently. This value can be calculated as follows:

$$d z = k \frac{l_c^2}{\Delta l} \tag{2.24}$$

where k is a constant value and takes the values 2 or 4 if a rectangular or a Hanning window is applied to the interference pattern. As with WSI, displacement along the z axis causes phase changes which can be measured by recording two images of the interference fringe pattern. In a linear approximation, the phase expressed as a function of l and z_j is given by:

$$f_j(l) = f_{0j} + \frac{4p}{l_c} z_j - \frac{4p\, z_j \Delta l}{N l_c^2}\, l \ . \tag{2.25}$$

where l ranges from l_c-$Dl/2$ to l_c+$Dl/2$. f_{0j} is the phase change introduced by reflection. The second term is the phase due to the optical path difference between the reference and jth surface at the central wavelength. Finally, the third term is the phase introduced by the changing wavelength as a function of the depth within the sample. Assuming that multiple reflections can be neglected, and representing the medium by N_s independent slices, the intensity recorded at each particular pixel neglecting the cross interference between scattering layers can be expressed in general form as:

$$\begin{aligned} I(l) = I_R + I_1 ... + I_j ... + I_{N_s} + 2(I_R I_1)^{1/2} \cos[f_{R1}(l)] + ... \\ + 2(I_R I_j)^{1/2} \cos[f_{Rj}(l)] ... + 2(I_R I_{N_s})^{1/2} \cos[f_{RN_s}(l)] \end{aligned} \tag{2.26}$$

where I_R, I_1, I_j and I_{Ns} are the mean intensities coming from the reference, surface 1, surface j and the last (j=N_s) surface respectively. f_{R1} is the phase difference between the reference and surface 1; f_{RNs} is that between the reference and the N_s surface. As in WSI, a 1-D Fourier transform is performed on $W(l)$ $I(l)$ where $W(l)$ is the 1-D Hanning window applied to each fringe pattern along the wavelength axis. Considering just positive frequencies, the amplitude spectrum will show the peaks coming from the dc term, and N_s peaks coming from the cosine terms. These peaks are centered on frequencies f_{R1} through f_{RNs}. An identical process is applied to the second fringe pattern. Once both fringe patterns are transformed to the Fourier domain and considering just positive frequencies the phase difference is calculated as

$$\Delta f_j = \tan^{-1}\left[\frac{\mathrm{Re}[\tilde{I}_1(f_j)]\mathrm{Im}[\tilde{I}_2(f_j)] - \mathrm{Im}[\tilde{I}_1(f_j)]\mathrm{Re}[\tilde{I}_2(f_j)]}{\mathrm{Im}[\tilde{I}_1(f_j)]\mathrm{Im}[\tilde{I}_2(f_j)] + \mathrm{Re}[\tilde{I}_1(f_j)]\mathrm{Re}[\tilde{I}_2(f_j)]}\right] \quad (2.27)$$

where $I_1(f_j)$ and $I_2(f_j)$ are the Fourier transform of the interference intensities before and after the deformation, respectively, and Re and Im denote respectively the real and imaginary part of a complex number. Df_j has values within the range -p to p, and is unwrapped in the usual manner along the *y* axis. Displacements can be calculated from that phase difference as follows:

$$w_j = \frac{l}{4pn}\Delta f_j \quad (2.28)$$

w_j is the resultant out-of-plane displacement component of the j^{th} plane within the medium, and *n* is the refractive index of the medium surrounding the scattering layers.

3. Experimental procedure

Considering that SOCT and DHI are different in their conception and model different set ups were developed. In this chapter a detailed description of the experimental procedure for each technique is described. Section 3.1 describes the optical system for metallic objects inspected with digital holographic interferometry. Section 3.2 describes the optical system for spectral optical coherence tomography.

3.1. Experimental set up for DHI

It was described previously that DHI needs a high resolution sensor in order to support loss of information when the Fourier algorithm is applied to obtain the phase. This is a significant difference between DHI and ESPI, which can achieve good results with low resolution cameras. There are some differences between set up of strain gradients and dependent strain gradients. The main differences are present in mechanical considerations and data processing. Section 3.1.1 describes Strain gradient experimental set up and section 3.1.2 continues with dependent gradient maps.

3.1.1. Strain gradient

For the case under study the object is illuminated with an Argon-Ion laser with a wavelength of 488 nm, from three different positions at a time, as figure 3.1 shows. The

use of this particular laser with that particular wavelength will provide an appropriate sensitivity for small loads.

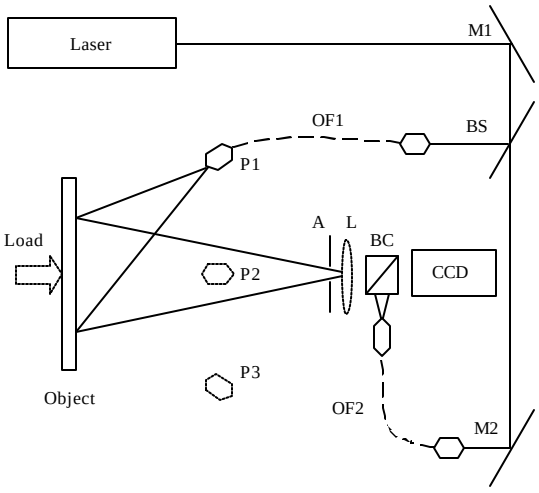

Figure 3.1. Out of plane optical set up for digital holographic : M1, M2, mirror 1 and 2; BS, beam splitter; BC, beam combiner; OF1, OF2, Optical fiber 1 and 2; A, Aperture; L, Lens; P1, P2, P3, Illumination positions 1, 2 and 3.

The reference beam is introduced on the CCD detector through a single mode optical fiber, whose length compensates the path length difference between the reference and object beam paths. An object image area is captured with a high-resolution CCD that has a sensitive area of 1280 by 1024 pixels at 12-bit resolution. The CCD sensor receives the reference beam and the scattered light from the object under study, and due to the coherent nature of the laser an interference process takes place. The optical system has a lateral magnification ~ 0.13 resulting in an object resolution of ~ 50 μm per pixel. For this optical method two images of such interference pattern are needed in

order to extract surface object displacements, i.e., one image for the object at any one state and the other with the load on the object. Digital holographic is best suited for the case under study, so as mentioned earlier both images are Fourier transformed [11, 56] to calculate their individual phase and on comparison a phase map is obtained which is directly related to the object displacement due to the load.

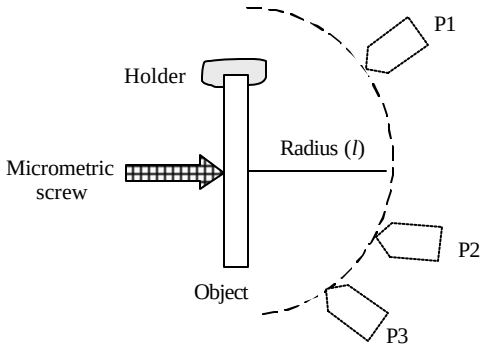

Figure 3.2 Imaginary sphere with minimum optical path difference: P1, P2, P3, are the object illumination positions 1, 2 and 3.

To produce the load on the object a micrometric screw is located just behind (not to be seen by the CCD camera, see figure 3.2) and in contact with it, in such a way as to have an arrangement that provides a repeatable and controlled object displacement, i.e., the object position is changed from an arbitrary base position to a displaced known one and then the micrometric screw is set back to the object base position. Many tests were performed with different displacements in order to find the base position. In this way fringes appear for the micrometer displacement and they disappear when the micrometer is set back to its original position. The latter is important in order to comply

with theoretical strain analysis assumptions (like small deformations applied). Experimentally it was found that a micrometer displacement of 5μm gives the best object recovery to its base position. To obtain 3D data from such object displacement, the object was illuminated from three different positions (left, center and right) as seen in figure 3.2, where an imaginary sphere was used to locate the three light sources in a position where they do not interfere with the field of view of the sensor. Considering this, illumination position number two (P2) is above the field of view of the camera. This configuration provides three pairs of digital holograms and hence three phase maps. It should be pointed out however, that it is not possible to determine ε_{zz} because the CCD sensor is along the z axis. Using the x and y displacement data both e_{xx} and e_{yy} are readily found. Figures 3.3a and 3.3b show two different surface contours, 40 by 40 mm with thickness of 8mm, of a metal object. The first one has a rather large dent in the center, while the second is flat (naked eye) without observable cracks on its surface.

(a) (b)

Figure 3.3 a) planar surface b) dented surface. Shows different sections from a metallic bar with thickness of 8 mm.

According with equation 2.8, figure 3.4 shows e_{xx} for the surface in figure 3.3a, with its contour drawn as continuous lines. The contour is a 2D representation from the object's surface height according with the point of view of illumination, obtaining lines with

same height. This full field surface strain map, represented by vectors, results from the data combination from every direction of illumination. The vector size is proportional to the micro strain magnitude present along the whole surface observed. As the magnitude of strain increases along the *x*-axis; contributions along *x* and *y* will have a stronger dependence on *u*. The orientation of the vectors depends on the derivative of these in-plane magnitudes. Coming from equation 2.9 e_{yy} is shown in figure 3.5 with a maximum surface strain of about 10e-6. This strain map remarkably shows an area on the surface where the strain is radial about a point. Figure 3.6 shows e_{xx} for the flat surface. The surface strain has a maximum magnitude of about 1e-6. The flat region is (naked eye), free of cracks and has a uniform contribution of in-plane magnitudes a feature expected for a metallic object like the one used here.

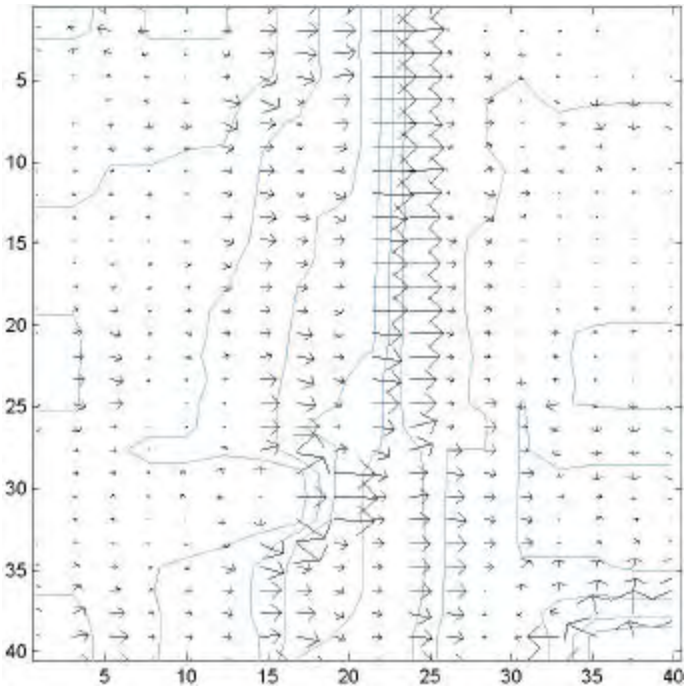

Figure 3.4 e_{xx} for surface in figure 3.3a

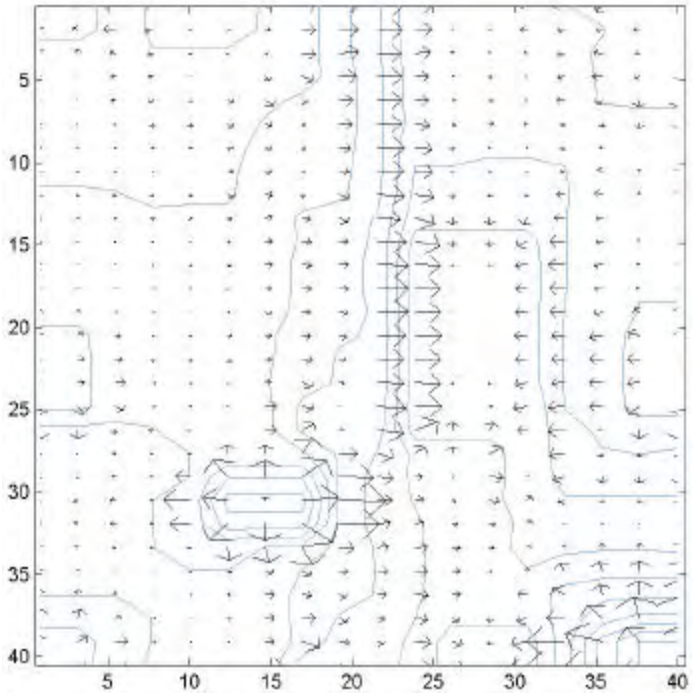

Figure 3.5 e_{yy} for surface in figure 3.3a

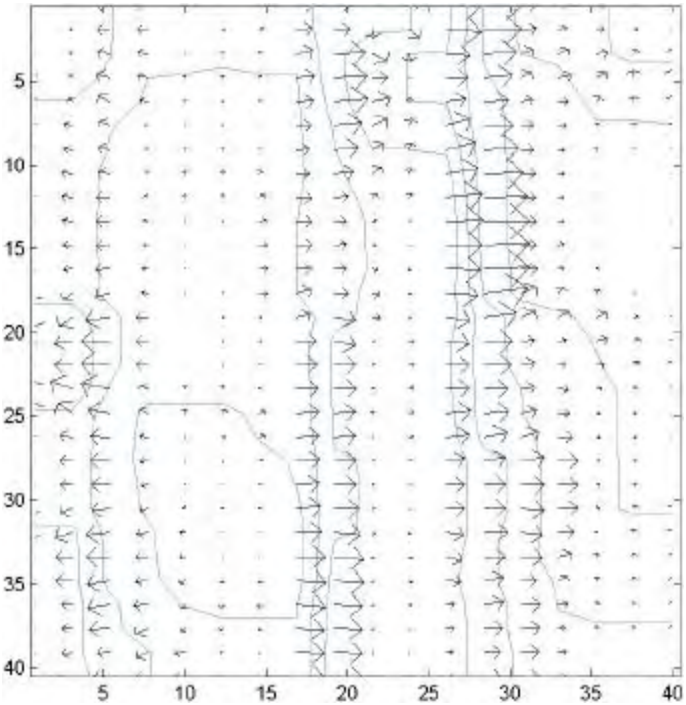

Figure 3.6e_{xx} for surface in figure 3.3b

Figure 3.7 shows an object surface, 30 by 60 mm, that presents a challenge since its relief may cast shadows when illuminated. To avoid this problem the center of the object is considered to be the center of a sphere with a radius l that coincides with the minimum (zero) optical path difference (opd) with respect to the reference beam, see figure 3.2. It is then possible to illuminate over the entire surface almost without any shadow problems. Once the three phase maps are obtained from all three illuminating directions the strain formulae are used to calculate the x and y gradients, e_{xx} and e_{yy}, shown in figures 3.8 and 3.9 respectively. The contour changes in its orientation, but not in magnitude, depending on the observation direction. Figure 3.8 and 3.9 shows a sparse vector map with central vectors revolving out of the page and larger strain detection close to the borders.

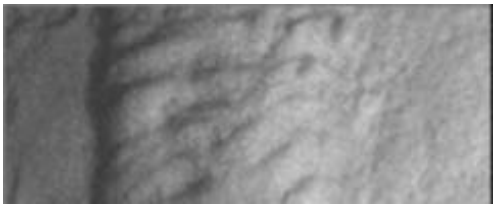

Figure 3.7 Surface with abrupt relief. Illumination array was performed in order to avoid shadows introduced from the central relief.

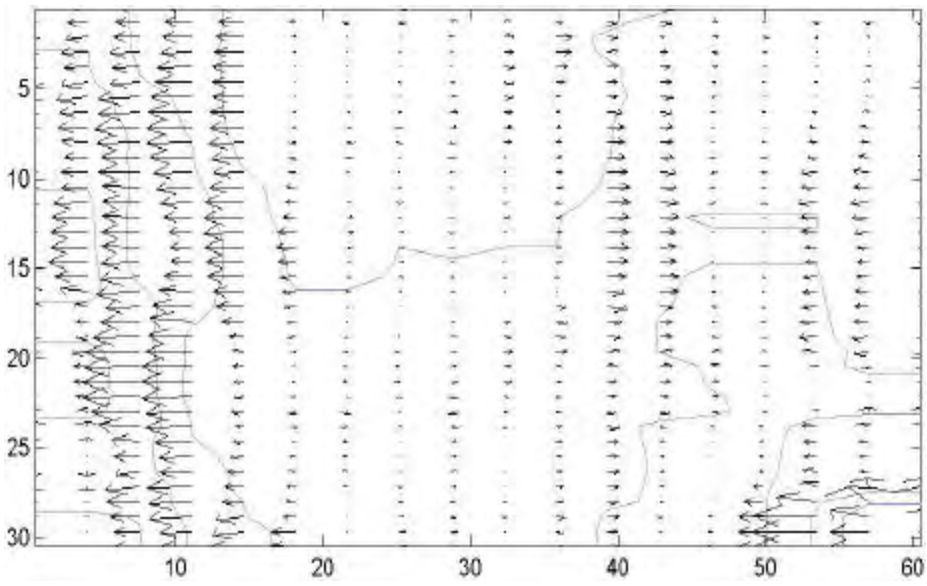

Figure 3.8 e_{xx} for surface in figure 3.7

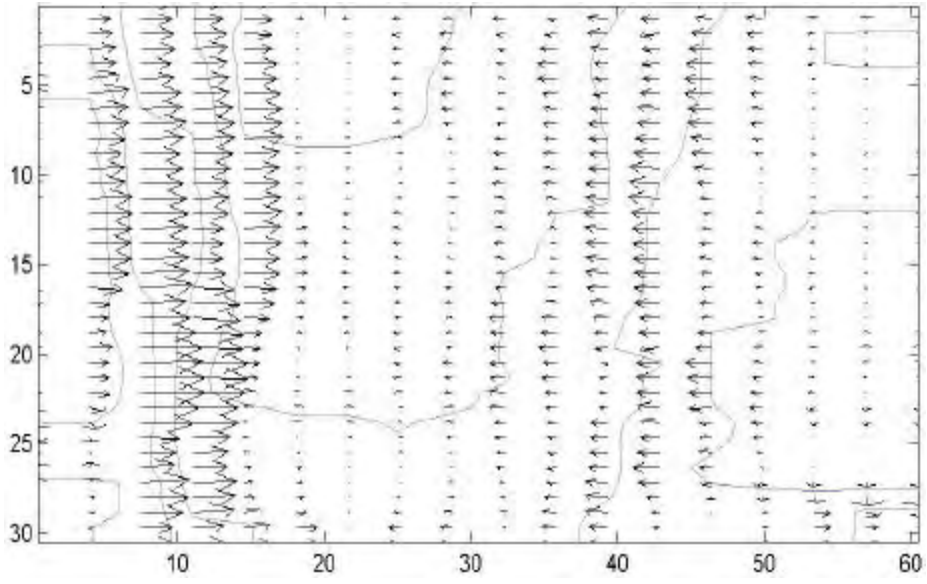

Figure 3.9 e_{yy} for surface in figure 3.7

3.1.2. Dependent strain gradient

The optical set up uses a Verdi laser CW (model V6 by Coherent) with a wavelength of 532 nm and a coherence length in excess of 6 meters (avoiding coherence length limitation when using the Ion-Argon laser), a feature that allows a large optical path difference between object beam and reference beam paths, was used to illuminate the object from three different directions (see figure 3.10).

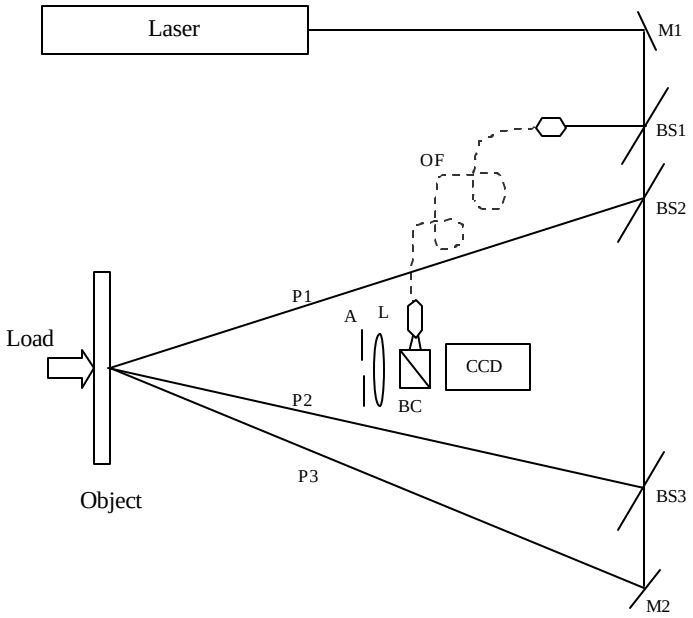

Figure 3.10 Optical set up for DH with multiple mechanical loads: M1, M2, mirror 1 and 2; BS1, BS2, BS3 beam splitters 1, 2, and 3; BC, beam combiner; OF, Optical fiber; A, Aperture; L, Lens; P1, P2, P3, Illumination positions 1, 2 and 3.

The reference beam is introduced into the CCD detector via a single-mode optical fiber. Similarly as described in 3.1.1, a high resolution CCD camera with a sensor area of 1280 x 1024 pixels at 12-bit resolution captures the image of the object. To obtain the

displacement components *u*, *v* and *w* two images are processed by subtraction for each one of the three illumination position with different states of the object, i.e., first state is with the object at its initial position (reference state) and the second state is with a known applied load (modified state). When one pair of image plane holograms are captured for a particular object illumination position, the other two object illumination positions are blocked so there is no light coming to the object from those directions. The three pairs of images are used to extract the phase map directly related to the object displacement caused by the load. The object is a thin aluminum plate, whose back, not seen by the CCD, was loaded by a micrometer screw driven with a computer controlled step motor. The accuracy of the strain measurement depends mainly on the precision of the load. To obtain a precise load, many tests were performed. Without load an image of the object is recorded, later, the load is applied and a second image of the object is recorded.

These two images are Fourier transformed to obtain their phase and a fringe pattern is generated. Leaving the object static in the modified state a series of images are recorded. This will generate a different fringe pattern in each case, then, with a subtraction algorithm of digital image processing any change in these fringe patterns with respect to the fist one may be seen. If a change is detected the step motor system moves to perform the needed correction. Only when all subtractions are zeroing the load system is mounted properly to the holographic table, and the load is ready to be applied. The step motor gives a circular movement with small increments of 0.02 degrees by step. A

mechanical arrangement was used on the motor to convert its circular movement into an out of plane displacement. The final mechanical system was able to apply a repeatable and controlled load. The load deforms the object in its elastically range, a feature that allows the recovery assumptions used in the theory. Considering that full field information of the object is observed, to display a dependent gradient map a three-dimensional mesh is generated to show the data processed. The algorithm generates this empty structure to make it possible to observe the strain magnitudes as a sparse vector map with direction with respect to x and y at any time, changing the mathematical assumptions in no way.

The object is a thin aluminum plate (area imaged was 30 x 40 mm, 1.4 mm thickness) whose smooth surface, plate 1 (figure 3.11), is not damaged and it does not present any dented region. This object is deformed in three different ways in order to detect different dependent gradients. The first is a centered out of plane load of 10μm, as mentioned applied behind the object. In this deformation the object is clamped in its vertical right edge leaving the left vertical edge free. The x and y strain gradient (e_{xx}, and e_{yy} respectively) are determined for this case and the generation of the x and y dependent gradient maps is then possible. To represent the dependent gradient maps, a field of vectors is introduced, where its size is proportional to the micro strain magnitude on that point. In all figures presented here the largest vector serves as the reference for the others, its magnitude its given for each case dealt with (see each figure legend). The direction of the vectors gives the direction where the strain is increasing or

decreasing, the larger is the vector the larger is the strain detected. Figures 3.12 to 3.15 show the four dependent gradients for this deformation, with the resultant three-dimensional deformation drawn on the object, given in micrometers.

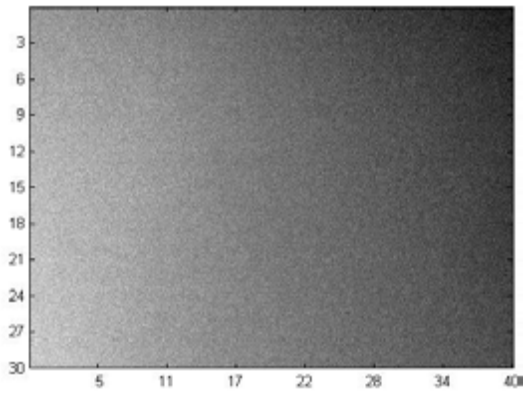

Figure 3.11. Observed area from plate 1. This object has no damage on its surface.

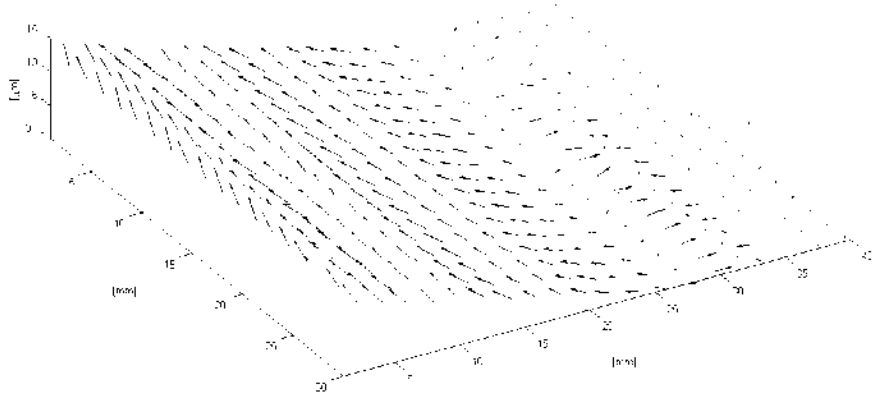

Figure 3.12. e_x (x) first deformation. The maximum micro strain value is of 75.8.

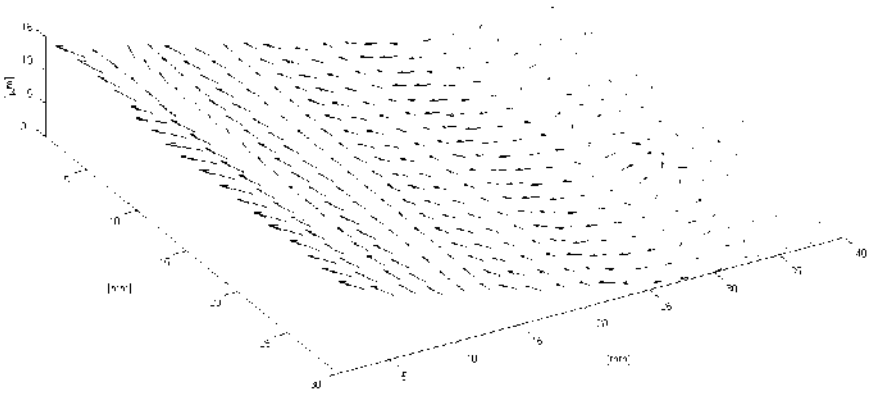

Figure 3.13. e_x (y) first deformation. The maximum micro strain value is of 98.7.

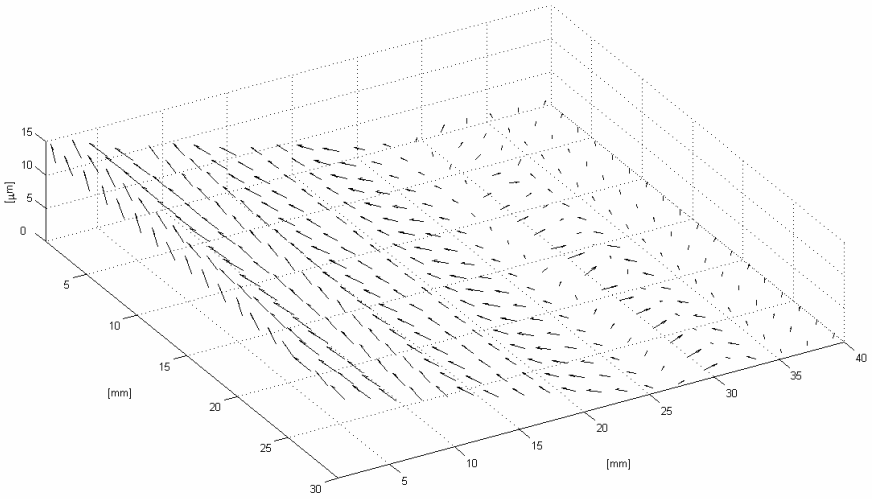

Figure 3.14. e_y (x) first deformation. The maximum micro strain value is of 54.4.

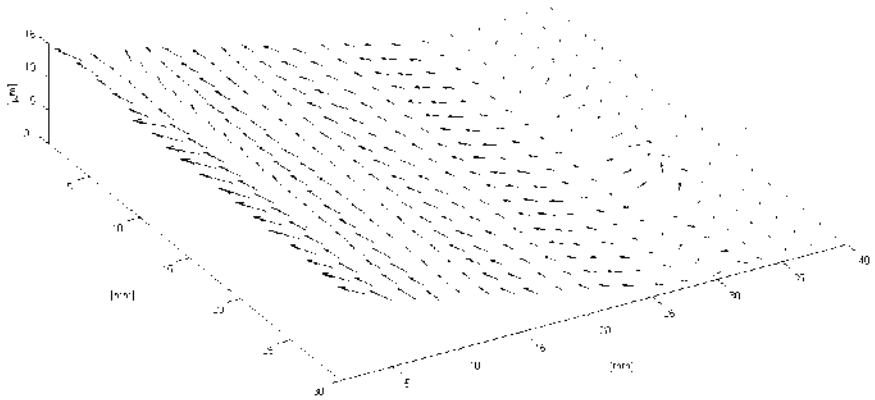

Figure 3.15. e_y (y) first deformation. The maximum micro strain value is of 53.4.

In this case the presence of the strain is mostly detected in the dependent gradients $e_y(x)$ and $e_x(y)$. The $e_y(y)$ is complementary for $e_y(x)$ but the surface strain is mainly present in the x direction with a maximum absolute value of 98.7 micro strains in this case. The same situation happens with $e_x(x)$ and $e_x(y)$ as seen for the same gradient map. Since this deformation is the simplest one and generates four maps with small differences among them. However due to the high sensitivity of the 3D DHI system and the amount of information gathered from it makes it possible to identify the small differences in each variable.

The second deformation applied to the same object is not centered on the y axis as the latter. In this case the deformation is applied 5mm below the upper edge and 10mm to

the left edge of the plate clamped in the same way as the first case. The displacement applied in that position is 10μm. Figures 3.16 and 3.17 show the $e_y(x)$ and $e_x(y)$ dependent gradients with a maximum micro strain of 119.9 micro strains with this deformation. These maps show a larger strain presence since this deformation introduced a larger object surface change. The vertical deformation in both maps show low stiffness object response in the *y* and *x* axes generating curved like surfaces.

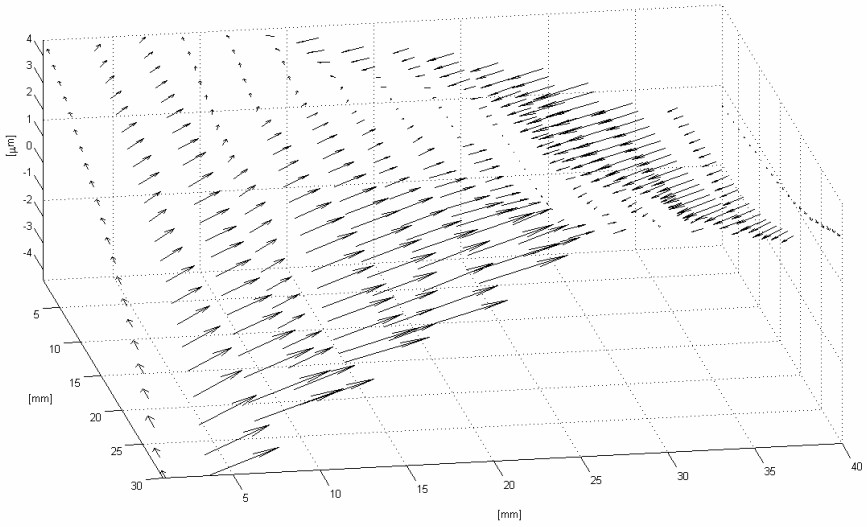

Figure 3.16. $e_y(x)$ second deformation. The maximum micro strain value is of 73.7.

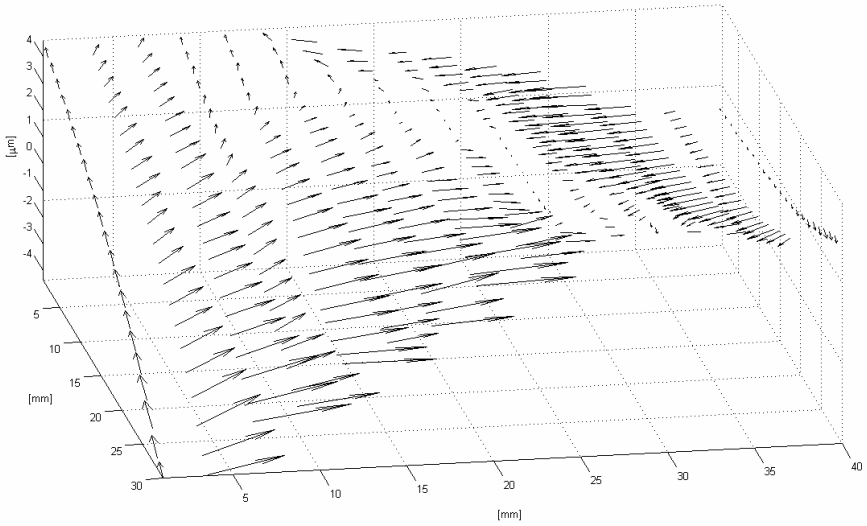

Figure 3.17. e_x (y) second deformation. The maximum micro strain value is of 119.9.

Like the first deformation, the surface strain is mainly present in the x axis even when a more complex pattern of strain is created. As figure 3.16 shows, there are two planes with head to head vector direction in the x axis due the deformation applied.

Finally, with the same object, a third kind of deformation is performed. To produce a bending on the object it is necessary to hold it by its vertical edges and apply a load in the middle. The load is a displacement of 10µm like in the first and second deformation. Figures 3.18 and 3.19 show the dependent gradient maps $e_y(x)$ and $e_x(y)$ respectively, where 462.6 micro strains are observed. Bending is observed in this case creating two maps with a high strain presence close to the center of the object.

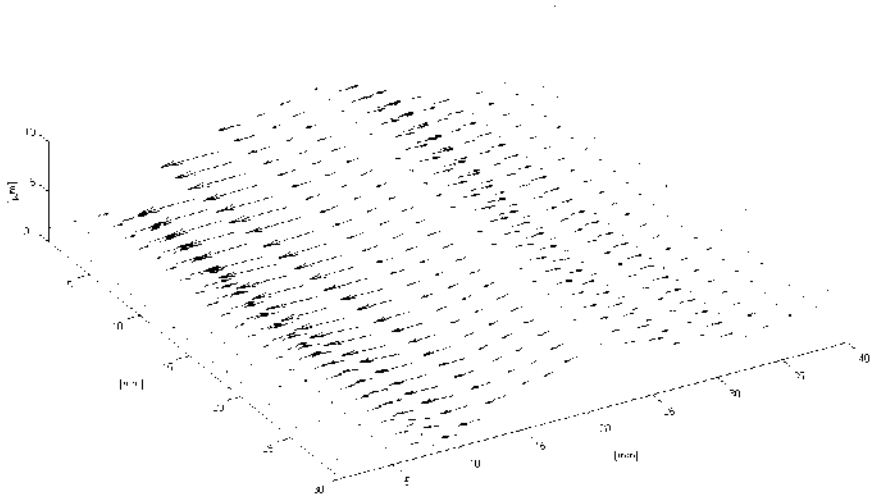

Figure 3.18. e_x (y) third deformation. The maximum micro strain value is of 462.6.

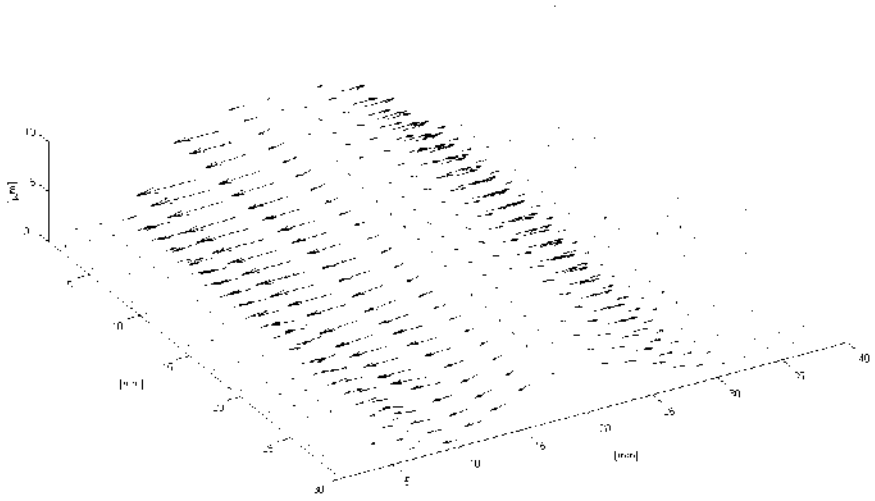

Figure 3.19. e_y (x) third deformation. The maximum micro strain value is of 388.5.

Figure 3.18 shows the maximum variation of the surface strain coming from the x gradient, and figure 3.19 shows the maximum variation coming from the y gradient. In all examples for plate 1, the cross dependent gradients $e_y(x)$ and $e_x(y)$, are more sensitive at any change of the surface strain. The isolation of these dependent gradient maps gives the possibility to detect the maximum variation of a gradient and a better analysis of it.

A thin aluminum plate with a smooth surface that presents variations in its shape along the *x* axis was studied, plate 2, shown in figure 3.20. The area under observation is 20 by 40 mm. This surface may be considered as to have a one-dimensional shape, meaning that a variation on its surface occurs along one axis (*x* in this case).

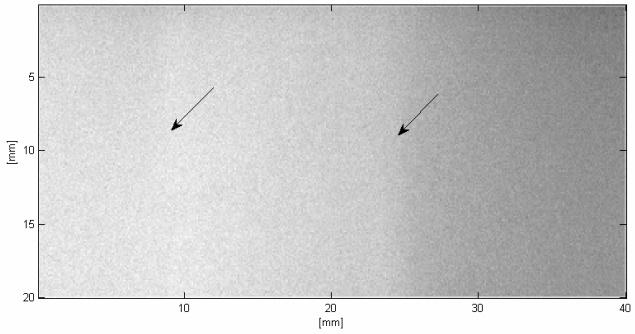

Figure 3.20. Image showing surface 2 with the irregularities shown with vectors.

The deformation is an out of plane load of 10µm applied in the center of the object clamped on one edge. Figures 3.21 to 3.24 show the four dependent gradient maps. The maximum value detected was 159.1 micro strains.

Figure 3.20 shows with the help of vectors, the location of irregularities on plate 2: all dependent gradient maps are able to detect them. Changes in magnitude are identified in $e_x(x)$ and $e_y(x)$ even when they are from different gradients. The components along the y axis are show in $e_x(y)$ and $e_y(y)$ in the direction where the object has no changes. In this case, all dependent gradient maps give a good estimation of the surface strain and its behavior. The large amount of information obtained from this technique is evident in these maps where high density vector regions are observed. For instance, changes in direction confirm the fact that plate 2 is not as flat as plate 1, in particular close to its edges.

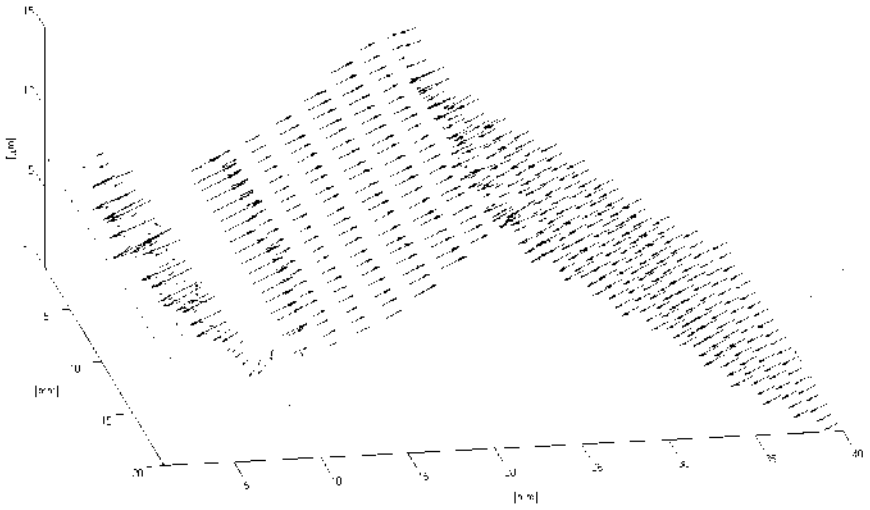

Figure 3.21. e_x (x) surface 2. The maximum micro strain value is of 115.3.

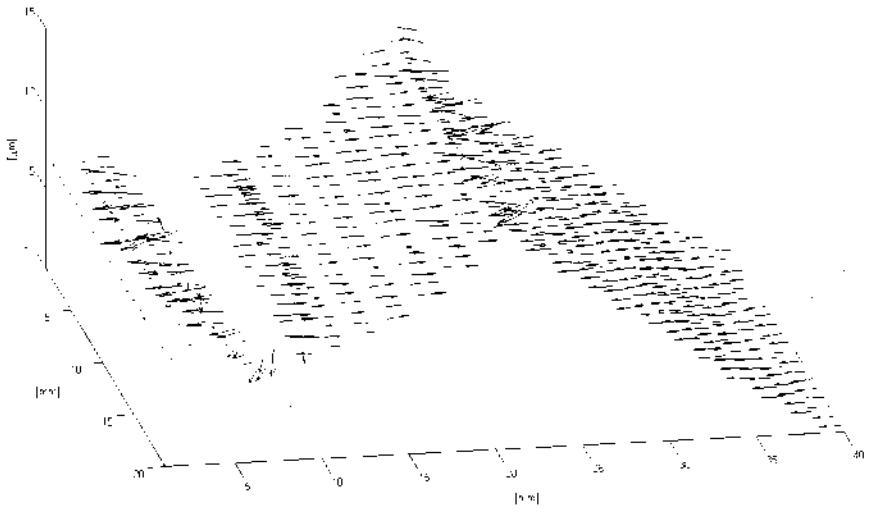

Figure 3.22. e_x (y) surface 2. The maximum micro strain value is of 80.0.

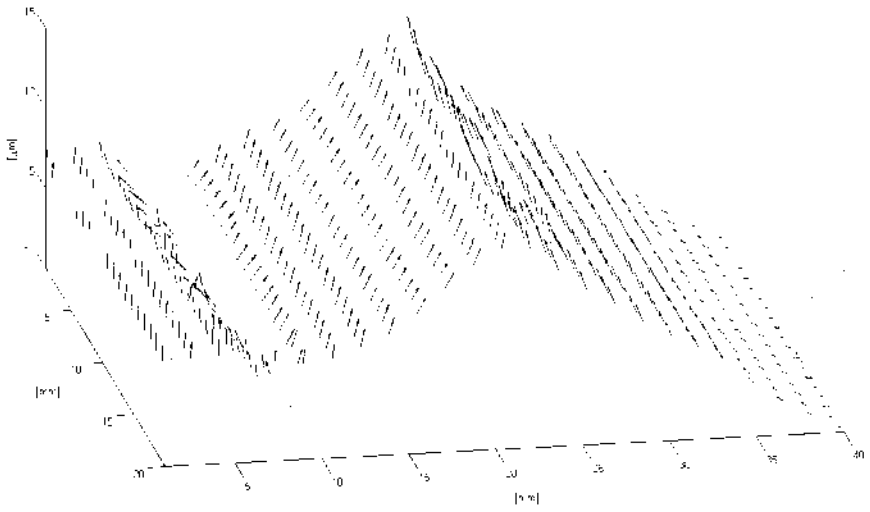

Figure 3.23. e_y (x) surface 2. The maximum micro strain value is of 159.1.

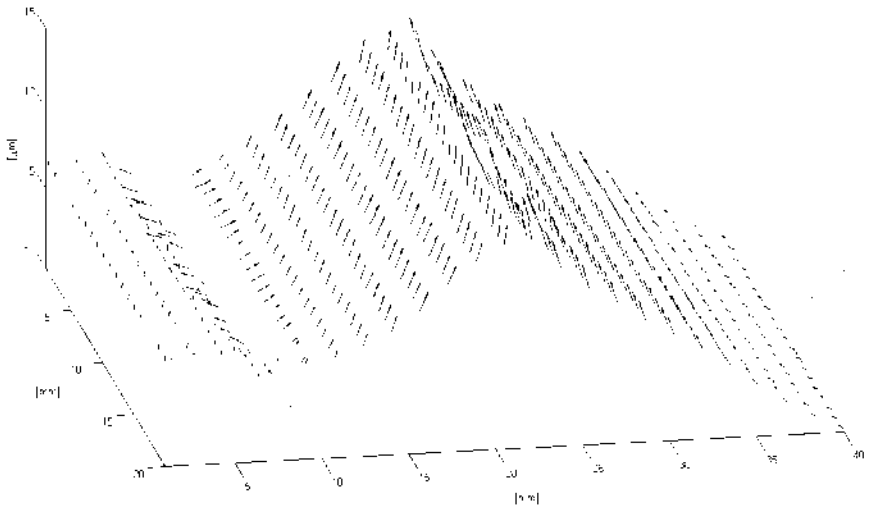

Figure 3.24. e_y (y) surface 2. The maximum micro strain value is of 145.0.

The DHI technique has the advantage to be whole field inspection, and not a point by point one, thus providing more data that is easily interconnected pixel by pixel. The dependent gradient maps may be analyzed with all information generated by the CCD or they can be sampled around the area of interest, e.g., figure 3.25 shows a small section for e_x (x) with the first deformation applied in plate 1 (figure 3.12). This area is about 1/48 of the full area observed there.

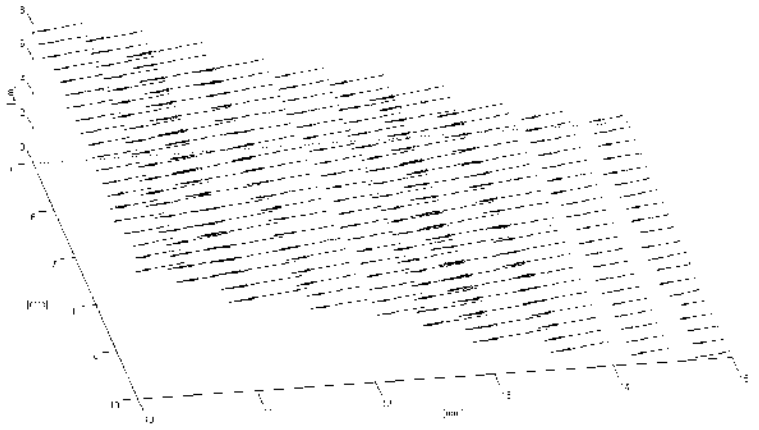

Figure 3.25. Section for plate 1 with first deformation ($e_x(x)$). The maximum micro strain value is of 36.0.

3.2. Experimental set up for SOCT

Several possible set ups have been proposed [35, 36]. A spectral system can be simple or complex depending on the application involved. In this case a double shot system with a sheet illumination is desired, this reduces possible set up options. According with this, the SOCT system is based in a Michelson interferometer, with a major difference on the kind of illumination source. In DHI and ESPI lasers are used to illuminate the objects. The laser can be considered as a monochromatic source that is well used in this kind of systems. But, these techniques do not penetrate into the sample, something desired in a SOCT system. The SOCT systems use a different kind of illumination which has a broad band source which has a short coherence length (see figure 3.26). A common device is a super luminescent diode (SLD) which has a stable response and can be found in different central wavelengths depending on the application. When a SLD illuminates a scattered media all wavelengths penetrate it (see figure 3.27), but how them interact with the sample changes. This response makes it possible to recover information at different depths (as was described in section 2.2.1). Considering that system is an interferometer, an interference pattern will appear according to the wavelength. Each wavelength interferes with its object and reference beam at the sensor (figure 2.8).

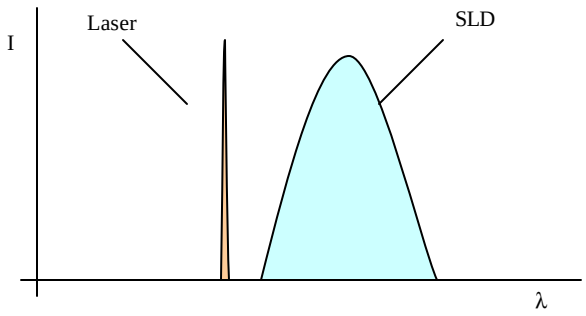

Figure 3.26. Spectral response difference between laser and a short coherence length source (like SLD).

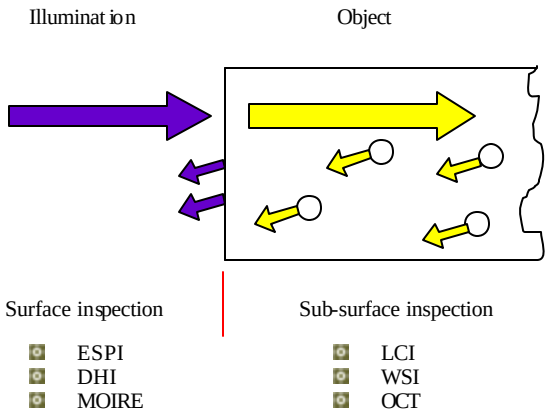

Figure 3.27. Penetration principle with a broad band source. All wavelengths penetrate the media. Internal reflections are coming from internal scattering.

The selection of a SLD and validation process is described in section 3.2.1. An application using organic samples is described in section 3.2.2.

3.2.1. Validation Process with the SOCT system

Considering that a SOCT system is based on the Michelson interferometer, figure 3.28 shows the basic concept of the optical system. But some points have to be solved before a final decision is made for the optimal configuration.

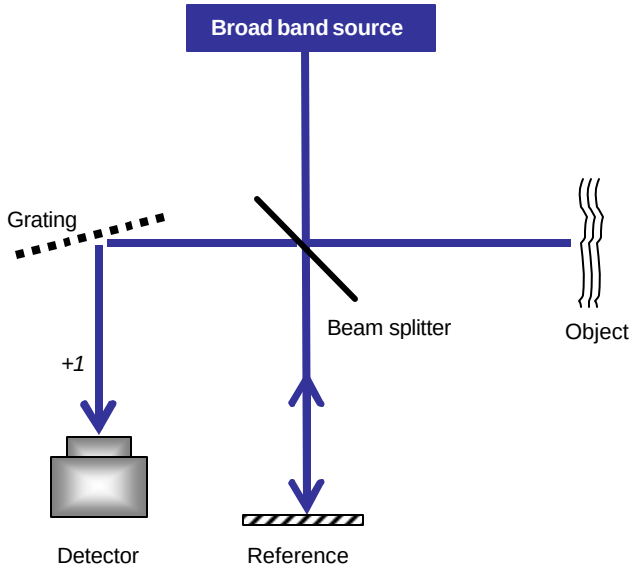

Figure 3.28. Basic concept for SOCT system.

The basic idea in an OCT system is to have slices of information for a three dimensional object. The slice has to be spread on the whole camera sensor. Measurements with the SOCT system are validated with a two beam interferometer embedded in the system. The first test includes a single mirror as the object in a simple configuration, see figure 3.29, where (CBS) is a cube beam splitter, (WBS) is a wedge beam splitter, (LCx) is a cylindrical lens (x=1, 2, 3) and (REF) is the reference mirror.

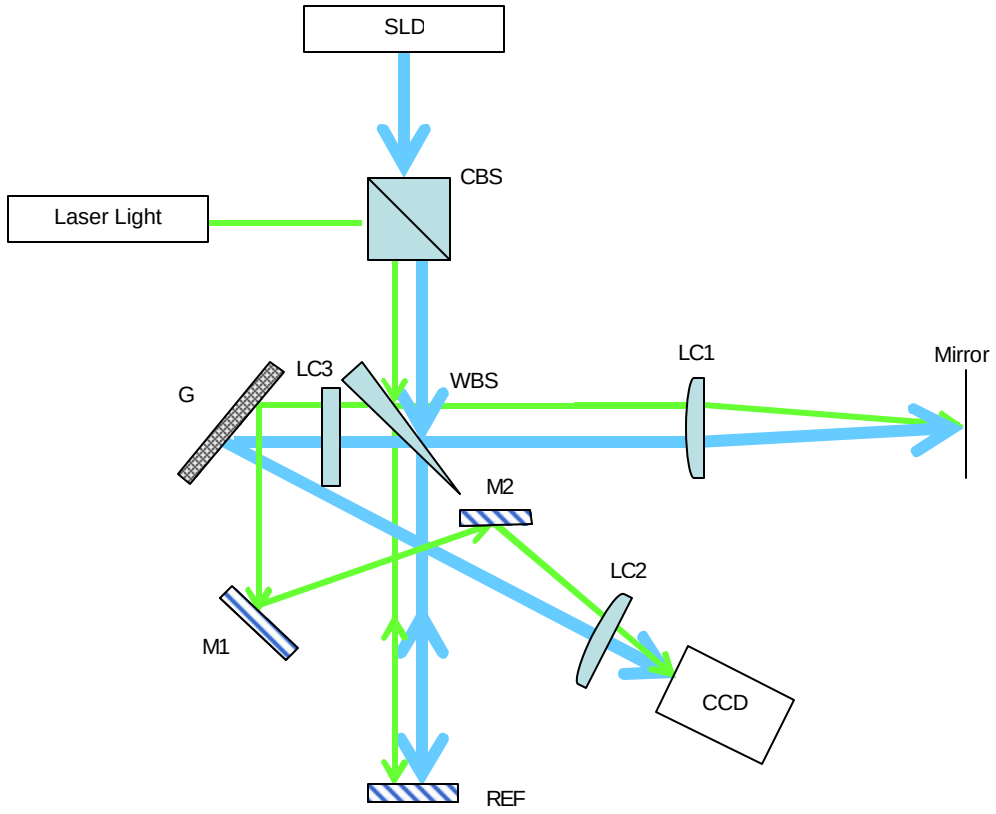

Figure 3.29. SOCT first test set up including a single mirror as object.
Both interference patterns are redirected in a single CCD sensor.

In this system, two light sources are used in order to have both interference present on the sensor. For this reason extra mirrors are needed (M1, M2) to redirect the laser reflection coming from the grating (G) which has 600 lines / mm.

With this set up it is possible to perform a scan while the object mirror is moved just a few micrometers using a micrometric screw. This test gives an idea of the system's sensitivity and how much can the object be separated from the reference mirror. After this test some considerations appear.

- Alignment is critical with the two extra mirror (M1 and M2) configuration.
- Multiple reflections introduce loss in front of CCD
- Quantum efficiency response of the camera is different for the laser and the SLD.
- Little diffraction angle coming from the grating with 600 lines/mm.

A second test is performed placing the sample mirror for a cover slip; and a second cover slip is included, generating three surfaces as samples because the second cover slip has a black paint layer on one side to avoid this reflection. In the frequency domain, three peaks are expected coming from the interference between the reference mirror and these three surfaces. Figure 3.30b shows the relative position of interference peaks according with their physical distances in figure 3.30a. First cover slip generates two interference peaks (RS1 and RS1') with the reference mirror and its two surfaces (S1 and S1'). Second cover slip generates just one interference peak (RS2) with the reference mirror and its surface (S2). Cross interference terms S1S1', S1S2 and S1'S2 are the secondary interference peaks among the cover slips surfaces S1, S2 and S1' without the reference mirror. Later means that a bigger separation allows higher frequencies moving the peak at higher frequencies zone (figure 3.30b).

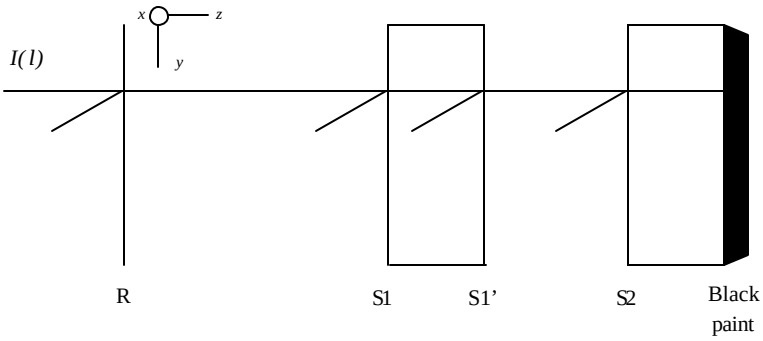

Figure 3.30 (a) Light propagation with three surfaces and reference beam.

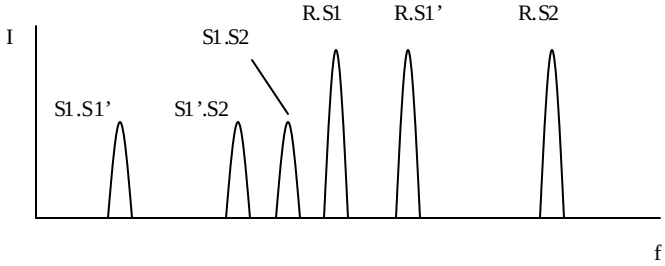

Figure 3.30 (b) Frequency spectrums with three surfaces and reference mirror.

This expected response was achieved with the previous system where the reference mirror is moved. Low intensity was detected considering losses of the system. Once the laser is introduced into the system, the optical path difference with respect to the SLD is different, but this just changes the magnification of the system, something to bear in mind. To avoid it later, the optical set up is modified: figure 3.31 shows a schematic configuration of the optical set up which is based on a Michelson interferometer with two sources of illumination.

One is a super luminescent diode (Superlum Diodes Ltd.) with a central wavelength of 840nm, bandwidth of 50nm and optical power of 15mW. The other is a CW laser (Lightwave 142) with a wavelength of 532 nm. Each beam coming from the sources was split into object and reference beams. The interference pattern from the SLD was recorded by camera C1 (Trust 380 Spacecam CMOS web cam 640×480 pixels at 8 bits), and that from the laser by camera C2 (Vosskühler GmbH HCC-1000 CMOS 1024×1024 pixels at 8 bits).

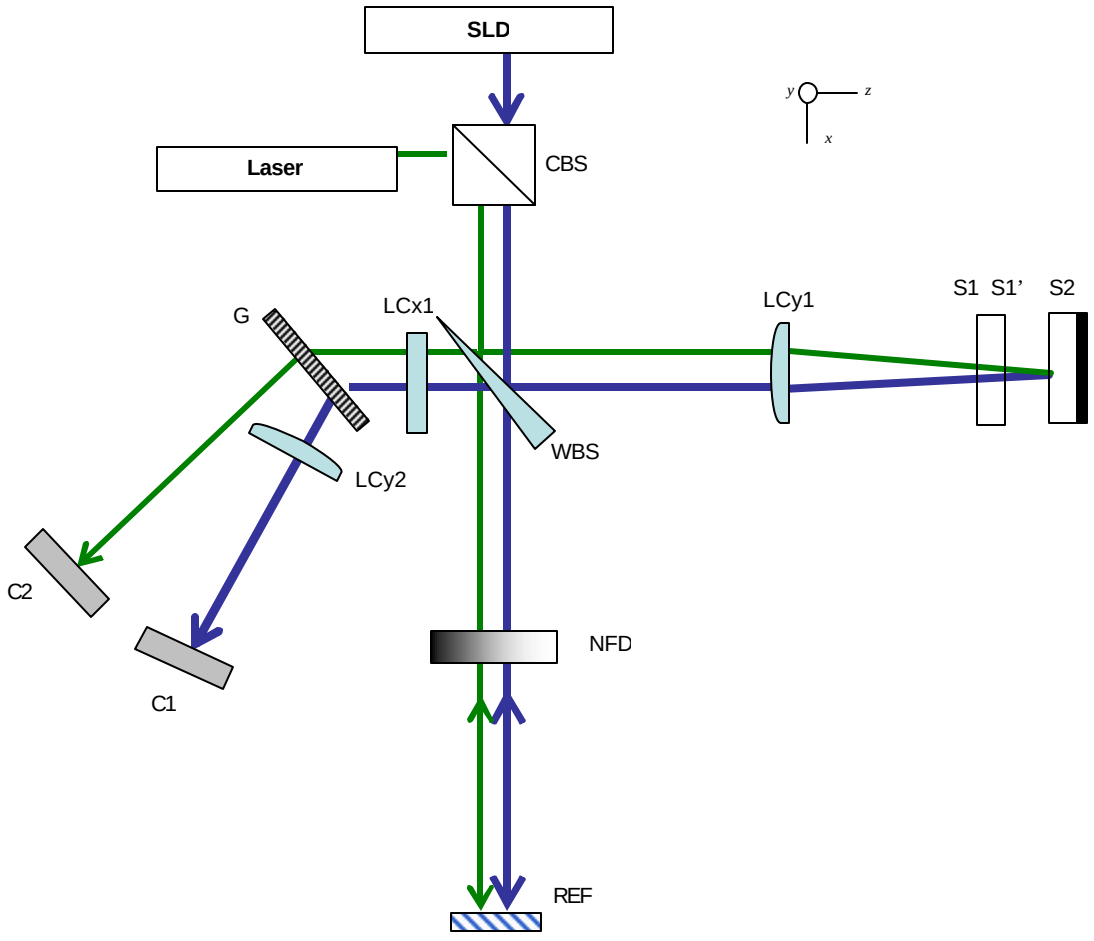

Figure 3.31 Optical set up used in validation process.

G is a transmission diffraction grating with 1200 lines/mm, NFD is a neutral density filter, CBS is a 50:50 cube beam splitter, WBS is an 80:20 wedged beam splitter and R is the reference mirror. Diffraction grating to image plane distances for both sources is the same. The wedged beam splitter is used to avoid spurious fringes due to multiple reflections from the laser and allowed the set up to be used with both the SLD and the laser at the same time. The test objects S1 and S2 were oriented normal to the *z*-axis within the depth range of the system. The first order diffracted beams from the two sources were spatially separated due to the difference in wavelength between them.

3.2.1.1. Illumination

To illuminate a narrow line on S1 and S2, three cylindrical lenses were used [57]. CLy1 and CLy2 were oriented with their axes parallel to the *y*-axis, and CLx parallel to the x-axis. The lens orientations are shown separately in the xz and yz planes in figure 3.32a and 3.32b respectively. The beams from the SLD and laser were initially collimated, so CLy1 generated a line parallel to the *y*-axis on the object at its focal length (fy1 = 100mm). Light scattered from the media re-entered the interferometer through the same lens. The combined object and reference beams passed through CLx which was positioned at twice its focal length (fx1 = 160mm) from the media. The SLD interference pattern was diffracted by the grating and CLy2 focused it onto C1 at its focal length of 160mm. The distance between C1 and CLx was 320 mm in order to set up a 4f system (see figure 3.32b). The laser interference pattern was diffracted directly

into C2, but no cylindrical lens was used here to spread the light from the monochromatic source on the full 2-D array. As complement figure 3.33 shows a three dimensional view of the optical set up where line propagation is showed.

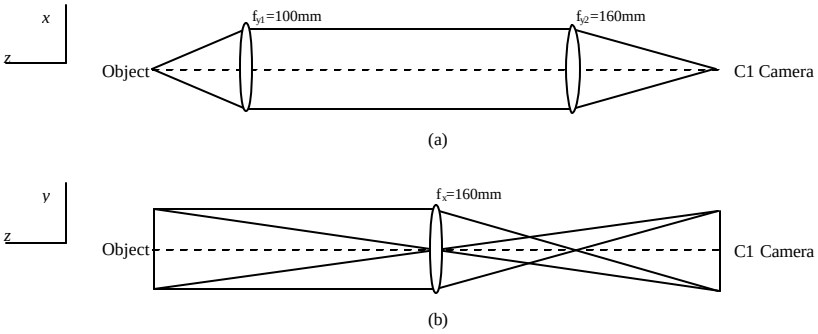

Figure 3.32. (a) x and (b) y-axis image formation.

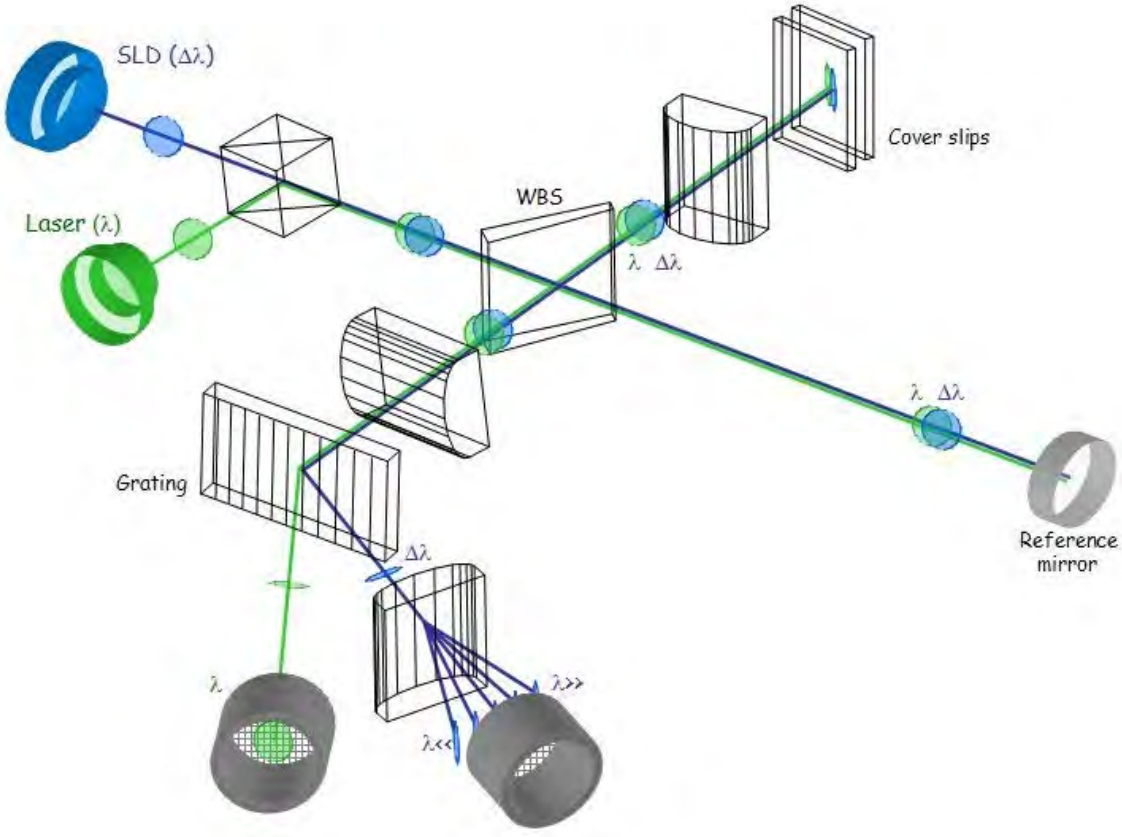

Figure 3.33. Three dimensional view of the validation set up. Laser emits a single wavelength and SLD emits a bandwidth.

3.2.1.2. Validation stages

In order to allow independent tilts to be applied to both surfaces, S1 and S2 were mounted in tilting stages whose angles were controlled by, respectively, three fine-pitch screws and three piezo-electric (PZT) actuators (see figure 3.34). The latter device was a highly repeatable tilting stage that made it possible to apply a tilt to S2 and then return it to its previous state, which was necessary for the measuring process described below.

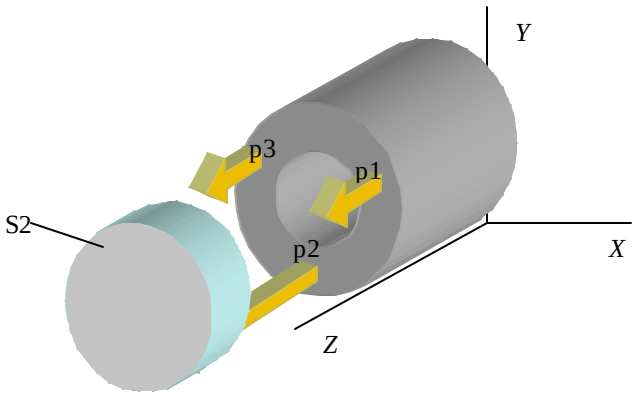

Figure 3.34. Burleigh piezo electric and S2. Independent and repeatable displacement p1, p2 and p3. In the validation process just p2 is used.

The following six-step recording process was performed so as to measure the displacement of the two surfaces at the same time (using SOCT) and independently (using standard two-beam interferometry as validation of the SOCT results). During the entire process the reference beam was present, as shown in figure 3.35.

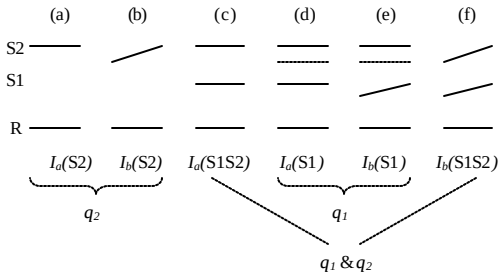

Figure 3.35. Experimental procedure for measuring tilt on S1 and S2 using SOCT, and validation using two-beam interferometry.

Subscripts a and b indicate states before and after tilting, respectively: (a) With S2 in its reference state, a laser interference pattern was recorded for S2, denoted Ia (S2); (b) After applying a tilt to S2, a second laser interference pattern was recorded for S2, denoted Ib (S2); (c) With S2 moved back to its reference state (a), S1 was inserted in its reference state and a first SLD interference pattern with both surfaces was recorded, denoted Ia (S1 S2); (d) A black screen was placed between S1 and S2 and a laser interference pattern was recorded for S1, denoted Ia (S1); (e) After applying a tilt to S1, a second laser interference pattern was recorded for S1, denoted Ib (S1) and (f) After removing the screen a second SLD interference pattern with both surfaces was recorded, denoted Ib (S1 S2).

The angles θ1 and θ2 in figure 3.35 are the tilts applied to each surface about the y-axis. Use of the black screen between S1 and S2 in steps (d) and (e) made it possible not to have a repeatable motion stage for S1 and thereby simplified the mechanical arrangement.

3.2.1.3. Validation results

Simple tests were performed on the sample consisting of two thin glass sheets to assess the performance of the proposed SOCT system. The objects were microscope cover slips with a thickness of ~300μm. S2 had a black paint layer on one side to suppress reflections from that side and was situated behind S1 (see figure 3.30a). The known thickness and refractive index (n = 1.5) of the cover slips were used to calibrate the system and to find the wavelength bandwidth Dl falling onto the camera (C1) detector by using equation 2.23. The bandwidth of the illumination falling onto the sensor was 25 nm. Using equations (2.21) and (2.24) the resulting depth range and depth resolution (with Hanning filter) were ~4.7 mm and ~110 μm, respectively. Figure 3.36a shows a fringe pattern from both cover slips where the λ-axis shows the range of detected wavelengths for the sensor. Figure 3.36b is the spectrum of the pattern along one line parallel to the λ-axis where frequency has been converted to optical depth through equation 2.23. The interference peaks for all surfaces are clearly visible and cross interference terms are well identified making it possible to filter them.

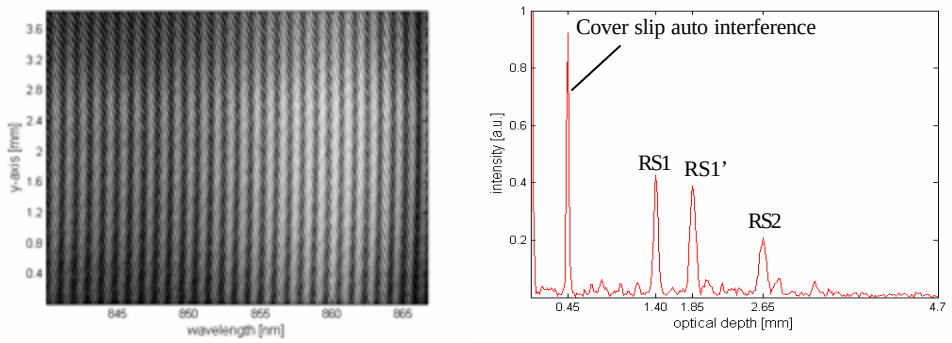

(a) (b)

Figure 3.36. (a) Interference pattern with both cover slips present, (b) spectrum of intensity along line y = 1.9 mm with frequency converted to depth by equation 2.23.

RS1 and RS2 are the interference peaks between the reference and surface 1 and 2 respectively. RS1' is the interference peak coming from the reference and the second surface of the first cover slip, S1'. However there are also peaks due to multiple reflections within the first cover slip. The cross interference terms have low intensity and these undesired peaks can be suppressed establishing a low threshold along the entire spectrum. The auto interference between S1 and S1' generates the first peak in figure 3.36b, located at an apparent depth of 450 μm, the same as the distance between RS1 and RS1'. These values coincide with the optical thickness of the cover slip. The depth resolution of the system is consistent with the expected theoretical value: the interface full width shown in figure 3.37a is 110μm after a threshold filter was applied at half the peak value.

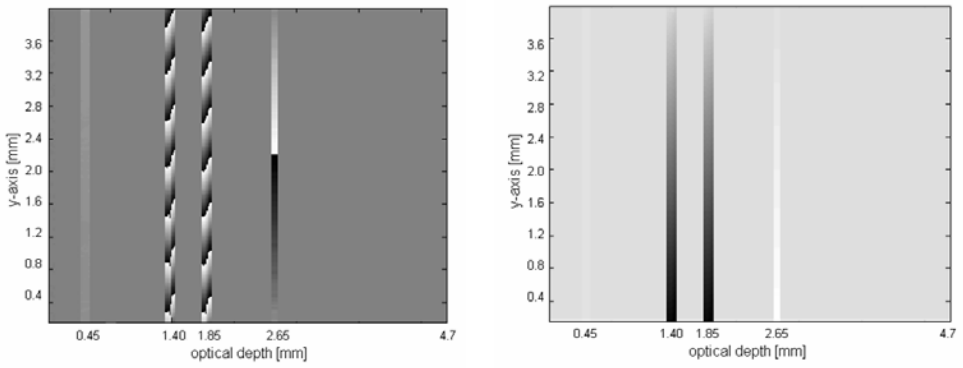

(a) (b)

Figure 3.37. (a) Wrapped and (b) unwrapped phase of the map difference representing out of plane displacement field at the interfaces shown in Figure 3.36(b).

Applying equation 2.27 to the interference patterns Ia(S1 S2) and Ib(S1 S2) from steps (c) and (f) of Section 3.2.1.2, the wrapped phase of the map difference is obtained for the entire medium as shown in Figure 3.37a. RS1 and RS1' have the same phase difference, as expected since they both come from the same cover slip. The phase difference measured at the auto interference peak (situated at 450μm) is also very close to zero for the same reason. Figure 3.37b shows the unwrapped phase map where tilt is clearly observed for each cover slip interface. RS2 has a smaller tilt than RS1 and RS1' due to the limited range of the PZT driver tilting stage. The unwrapped phase map is then converted to displacement at each interface using equation 2.28.

Figure 3.38 shows a comparison of the displacement profiles measured at each surface by means of phase-contrast SOCT and two beam interferometry using images Ia(S2), Ib(S2), Ia(S1) and Ib(S1) acquired by camera C2 during steps (a), (b), (d) and (e). Two

beam interference images contained a narrow band of fringes due to the monochromatic light source and were converted to phase using the Takeda Fourier transform method [38] applied along the y direction. Tilt angles measured with phase-contrast SOCT for S1 and S2 were 771 µrad and 114 µrad respectively, compared to 767 µrad and 113 µrad obtained with two beam interferometry. Respective errors of 0.5% and 0.8% for the two surfaces can be regarded as in very good agreement.

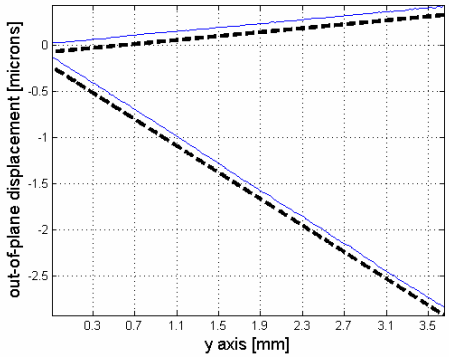

Figure 3.38. Displacement field profiles measured using phase-contrast SOCT (solid lines) and standard two-beam interferometry (dashed lines). An arbitrary offset of 0.1µm has been added for clarity.

Two beam interferometry with laser takes one line of the fringe pattern and considering that the objects are thin glasses Takeda method to obtain the optical phase is a good option. Phase calculation is performed in the usual manner:

$$j_{u1} = \arctan\left(\frac{imag(F_1^{-1})}{real(F_1^{-1})}\right) \tag{3.1}$$

$$j_{u2} = \arctan\left(\frac{imag(F_2^{-1})}{real(F_2^{-1})}\right) \tag{3.2}$$

F^{-1} means inverse transform applied to first and second interferogram. Once the wrapped phase map is obtained, an unwrapping algorithm generates the unwrapped phase map. The phase difference will be then,

$$\Delta j = j_{u1} - j_{u2} \tag{3.3}$$

where j_{u1} and j_{u2} are the phase information coming from both interferograms. The same procedure as SOCT system is taken to determine the field of view to find the tilt applied to the object.

3.2.2. Phase detection in organic media

Once the SOCT system has been validated it is possible to start an exploration in a more complicated media. Highly potential area for the applications is the medical one. Using the same SLD with 840 nm a pig cornea was inspected. This wavelength gives a good estimation of system's sensitivity considering high water absorption for this wavelength. The optical set up was modified in order to have this cornea in the interferometer as shown figure 3.39. The optical magnification of this system is one. Grating efficiency is about 55% with no polarized light. The reference mirror is an ion silver coated mirror to keep the system with the minimum absorption. The cylindrical lens in front of the CCD

camera has a focal length of 160 mm in order to have the whole diffracted light in it. The detector in this case is a CCD camera 12 bit VDS QBF 1300 (Vosskühler GmbH).

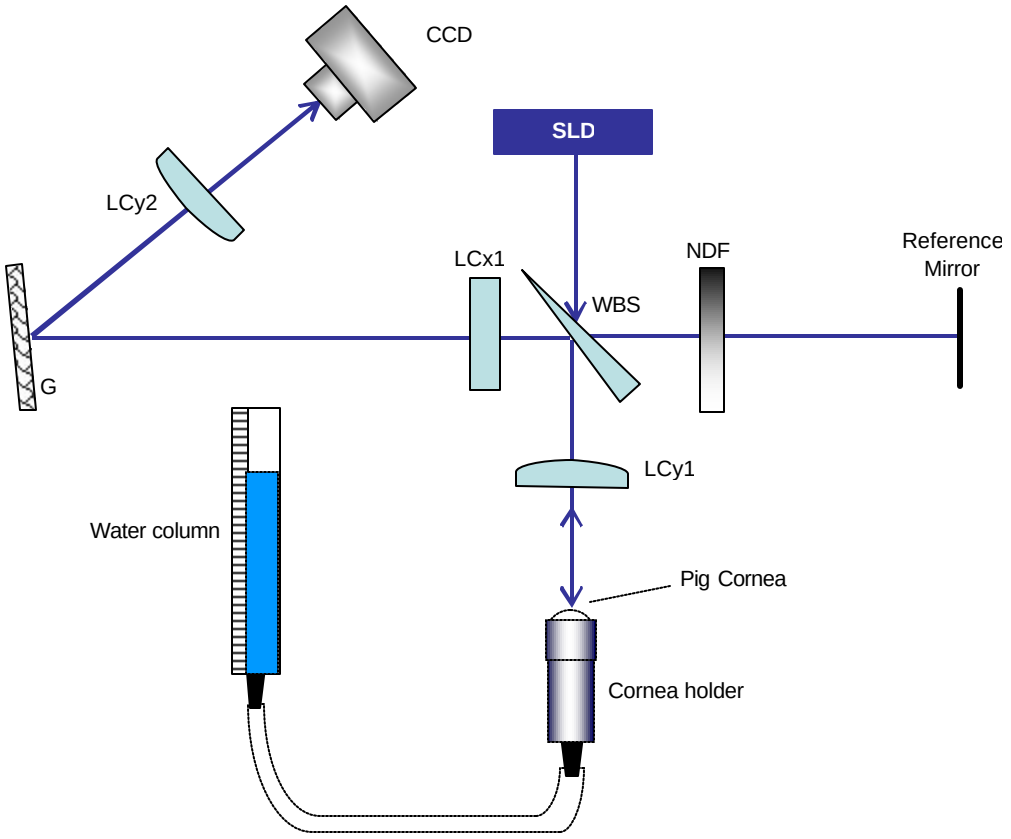

Figure 3.39 Optical set up for pig cornea inspection.

3.2.2.1. Cornea structure

The cornea has three principal functions: it protects the inner contents of the eye, it maintains the shape of the eye, and finally it refracts light [58]. Any disease or injury changes these functions, it gives great importance to know the biomechanical properties

of the cornea. Cornea structure (see figure 3.40) has two unicellular structures covering it and a group of laminar cells called stroma. The epithelium is the most external layer of cornea and has a high mechanical stiffness. The stroma is the inner region of cornea and has an array of laminar cells that allows light transmission into the eye. This particular distribution of stroma avoids any distortion in image formation and gives high mechanical resistance (see figure 3.41). This is the major reason to consider the cornea as transparent media. The last layer of cornea is the endothelium which is a unicellular layer similar to the epithelium.

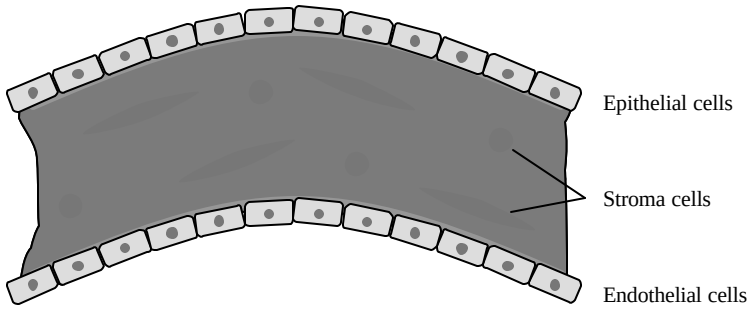

Figure 3.40 Cornea structure. Normally, cornea width is ~ 800 micrometers.

Figure 3.41 Stroma laminar structures showed. This distribution avoids optical distortion while light travels trough cornea keeping it as transparent media. ©J. Royal Society

3.2.2.2. Camera selection

The CCD QBF-1300 has a larger dynamic range than the HCC-1000 used in the validation process. But more important is not to have any layer in front of the sensor in order to avoid fringe introduction coming from auto interference in this layer. The CMOS camera HCC-1000 introduces circular fringes. These fringes are an auto interference coming from a thin layer optimized just for the visible wavelengths. This layer Schott D-263 glass (borosilicate glass) is in front of the CMOS sensor, with thickness of 559 µm ± 51 µm, and there is an air gap before the sensor of 457 µm ± 102 µm as shown in figure 3.42. This glass has a transmission factor flat enough from 400 to 2600 nm (see figure 3.43). The refraction index is ~ 1.5354 with an Abbe number of 55. Considering the presence of this layer it is possible to have the CMOS camera working with the system and these fringes will stay static during the entire test. But a posterior data processing will introduce losses and the dynamic range will decrease.

According with this, the reduction is coming from the sensor which has a quantum efficiency lower in the near infrared, going to zero at 1000 nm (see figure 3.44). For all these reasons the CCD camera (12 bits) was used instead the CMOS camera (8 bits). Some tests with fresh drop of paint are performed and the system is able to detect it. But in order to have organic objects under study, the first organic test is performed with an onion skin.

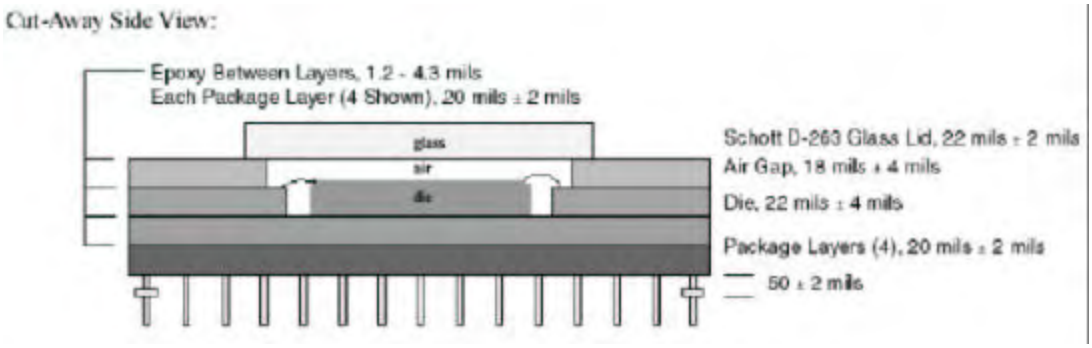

Figure 3.42 CMOS sensor drawing of HCC-1000 (Photobit Corp.)

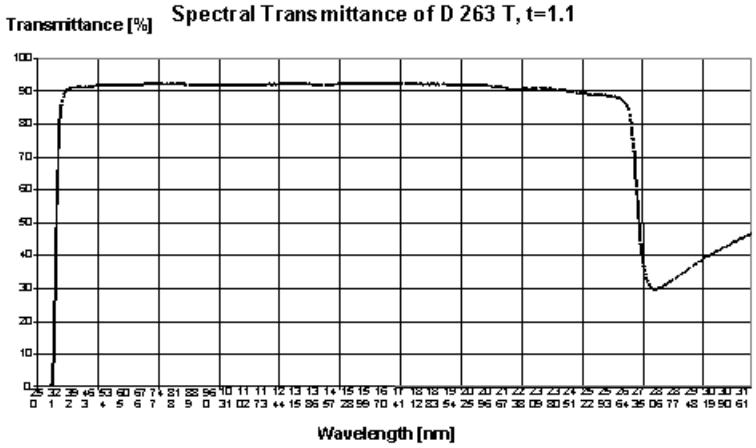

Figure 3.43 Spectral transmission of D-263 (SCHOTT North America, Inc.)

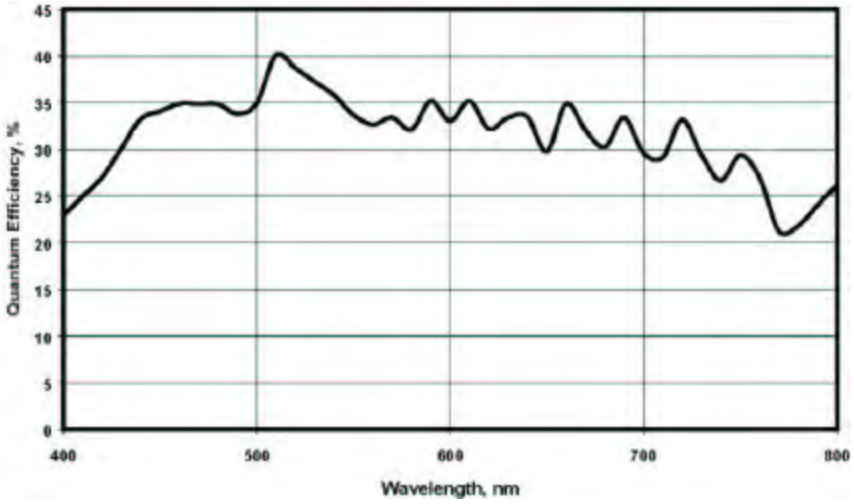

Figure 3.44 Quantum efficiency of CMOS camera HCC-1000. Decrease linearly to zero at 1000 nm. (VDS Vosskühler GmbH, Germany)

3.2.2.3. Organic samples

Organic tissues absorb much of the IR radiation that is applied. Considering this, the optical set up was re engineered to maximize its performance within the technological limitations of the equipment. The cylindrical lenses are orthogonally aligned to increase the visibility and contrast. First experiments with the SOCT system were performed with thin glasses (cover slips), which do not change considerably the polarization coming from source of illumination. Figures 3.45a and 3.45b show the same section of fringe patterns with a reference mirror and a cover slip with and without polarization filter.

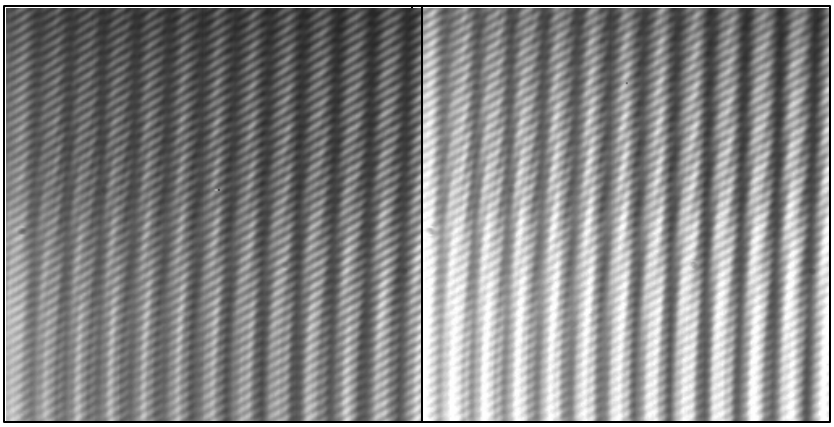

(a) (b)

Figure 3.45 (a) with polarization filter (b) without filter.
Both images have the same exposure time of 8.7mseg.

In organic tissues the light scattered from inside the object has a depolarized effect in all directions which compromise the modulation of the fringes. Then, polarization filters are placed in the object and reference beam paths. Placing these filters cause the

intensity to decrease, but the modulation is more notorious and the dc term and the cross interference are well identified far from the object information. Figure 3.39 shows the optical set up which has an optical magnification of 1. Light coming from the object is recorded into the sensor with a relation 1 to 1. Using different regions of an onion skin was found that there are some samples containing excess of water and they are very difficult to see with the SOCT system.

Considering bibliographic references that used onion skins in their optical set ups magnification factor of those systems have to be increased. Considering that the cylindrical lens in x will be the same one, with a focal length of 160 mm, taking equation 3.4,

$$\frac{1}{f} = \frac{1}{Si} + \frac{1}{So} \tag{3.4}$$

where f is the focal length, Si and So are the image and object distances respectively. Optical magnification of a system is giving by:

$$m = \frac{Si}{So} = \frac{hi}{ho} \tag{3.5}$$

where hi and ho are the image and object height respectively, according with physical measurements of the system the largest magnification is ~2.3 with So = 230 mm and Si = 526 mm, as shown in figure 3.46. This plot was generated with equation 3.4 considering a f = 160mm. According to this plot, the system is reallocated to have a magnification of 2.3 and considering that sensor has a size of 10mm the maximum size in the object plane is going to be 4.3 mm.

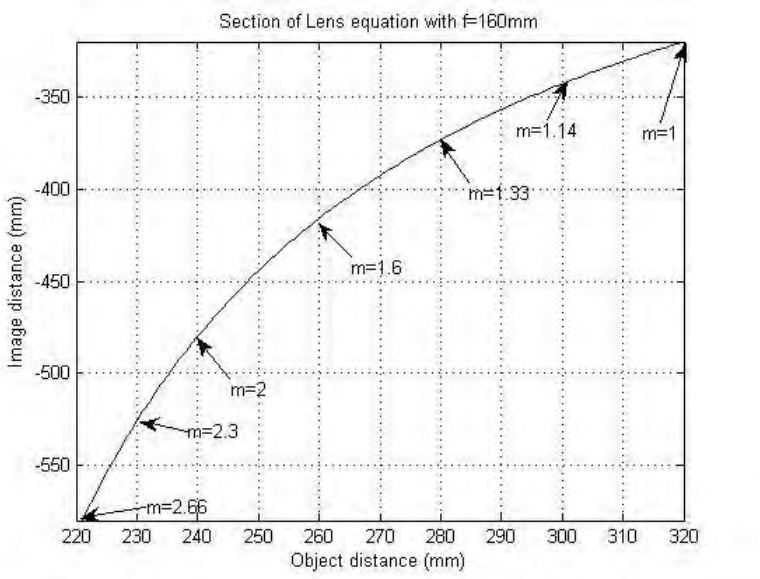

Figure 3.46 Plot of lens equation to determine maximum magnification allowed with the system. Value of *So* is physically limited to 230mm max.

After several tests the CMOS camera reduces the modulation of the fringes even in well know objects like mirrors and cover slips. Figure 3.47 shows an image with a cover slip. This image shows clearly the noisy signal due to reference acting with the glass of the camera. Introducing a tilt on the camera clear the signal slightly, but the modulation decreases considerably.

Different samples are tested using a web cam instead of the CMOS camera (see figure 3.48) with magnification 2.3. These images are the first approximation to penetrate inside the kind of objects like the ones dealt with here. Preliminary results show high sensitivity and the camera is changed again to increase the dynamic range (96 dB) of the system with the CCD QBF-1300.

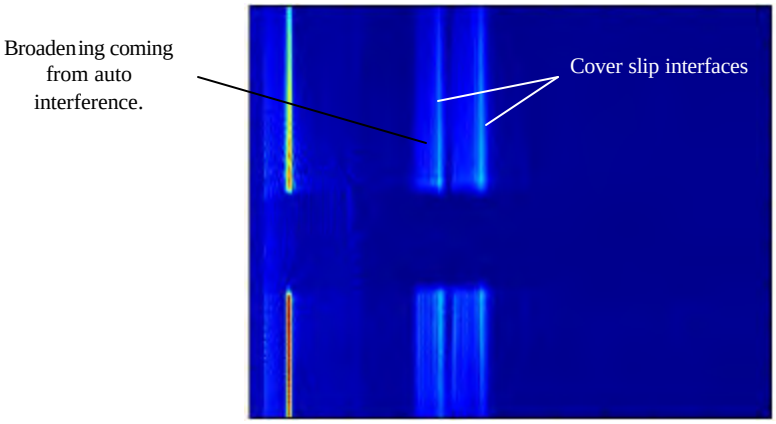

Figure 3.47 Intensity image with CMOS camera showing noisy signal coming from its protective glass. CMOS camera dynamic range of 48 dB is reduced considerably with this noise.

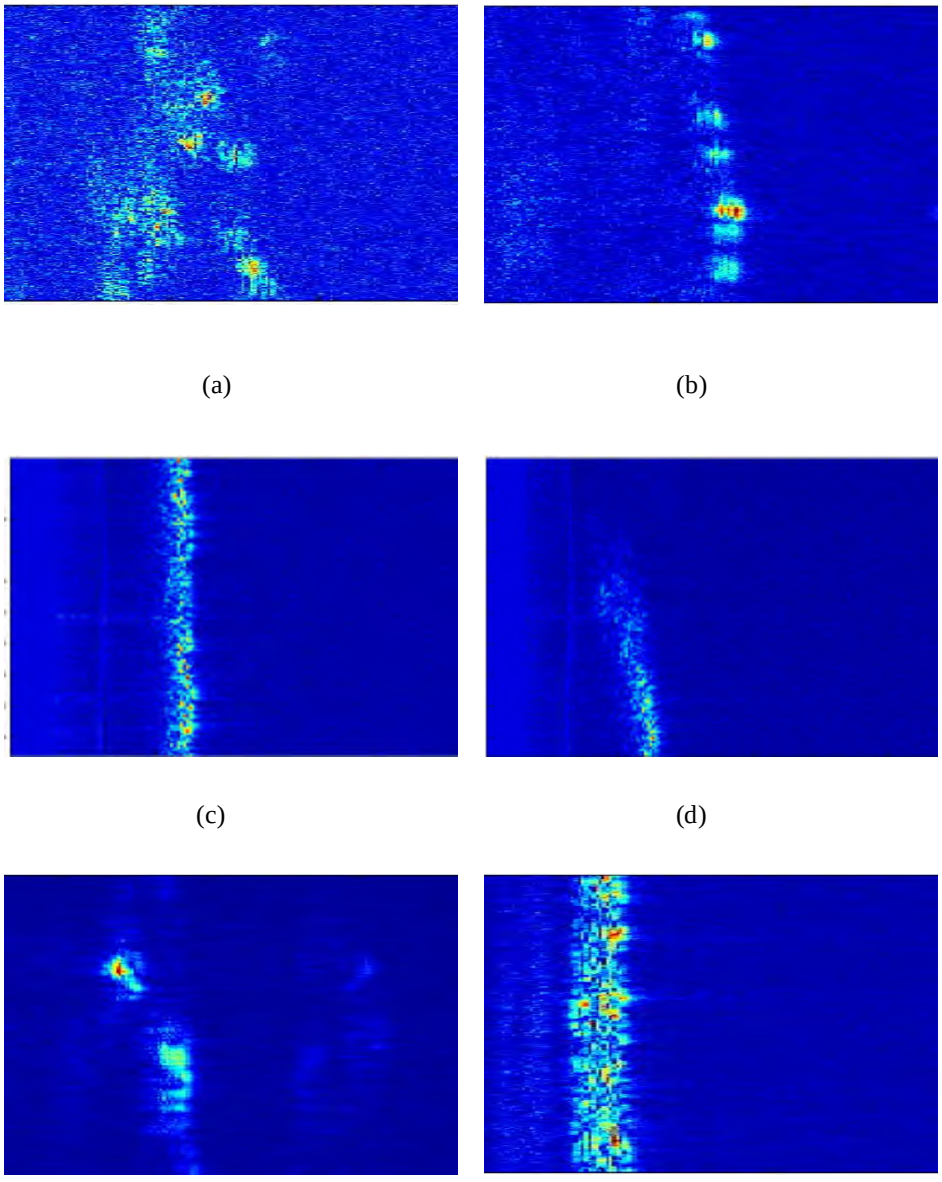

(a) (b)

(c) (d)

(e) (f)

Figure 3.48 Images of (a) sponge (b) dry onion (c) toilet paper (d) broken toilet paper (e) rubber and (f) adhesive tape

To test the pig cornea some considerations need to be taken. The optical set up needs a mounting in order to have the hydro static test. The cornea mounting is designed to hold perfectly the pig cornea avoiding any water outflow. The system will have a vertical cornea mounting, meaning that the optical set up is moved closer to the edge of the holographic table.

The hydro static load will apply a constant load behind the cornea that will make it possible to simulate the internal pressure in the eye [59]. The mechanical mounting designed for this purpose is shown in figure 3.49 (all values are in millimeters).

The rig holds the cornea resulting in a membrane easy to load with a saline water solution. This solution can be 15 mg. of salt dissolved in one litter of water or a soft contact lens solution. A previous review in references suggests that a little pressure is well detected onto the cornea. Pig cornea has a very similar behavior to human cornea under this kind of tests. In first instance just using a tube moving it vertical will apply the load of water in the system.

Conversion function of millimeters of water into pressure units (Pascal) is needed. This relation is 1 cm of water is equal to 98.0665 Pascal. First tests with cornea were performed at normal ocular pressure (~4kP). Figure 3.50 shows an intensity map with a cornea showing scattering coming from the epithelium and stroma.

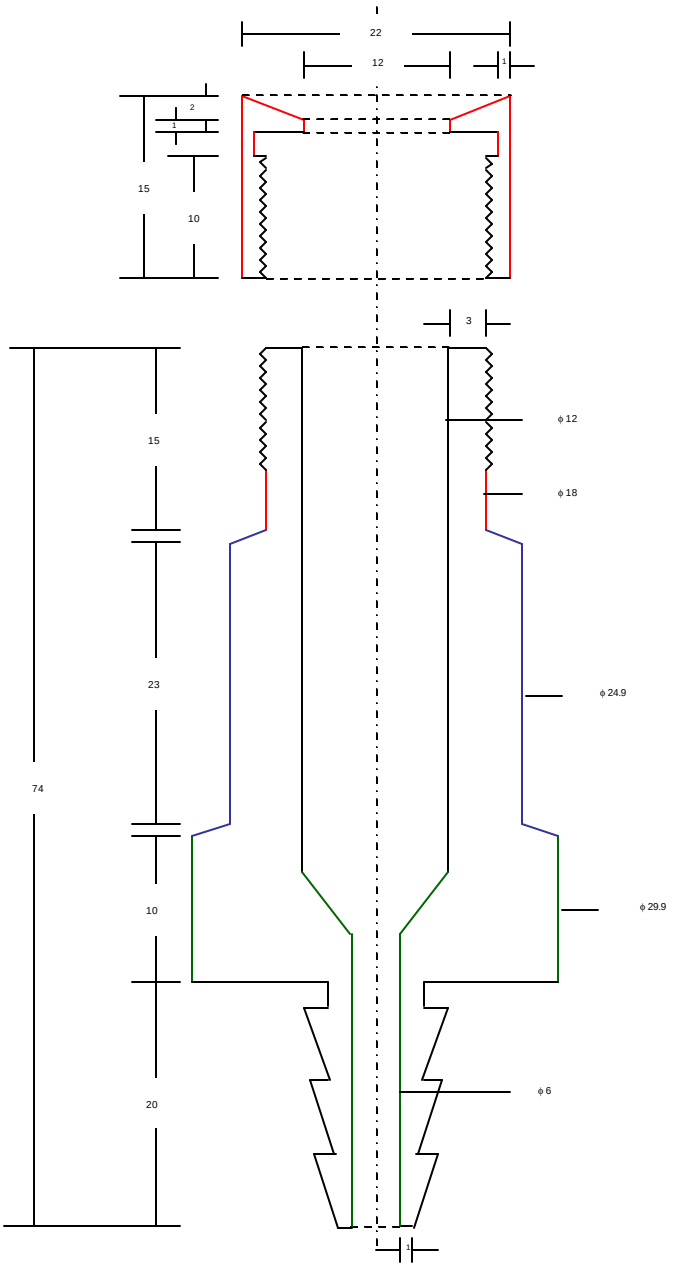

Figure 3.49 Pig cornea mounting.

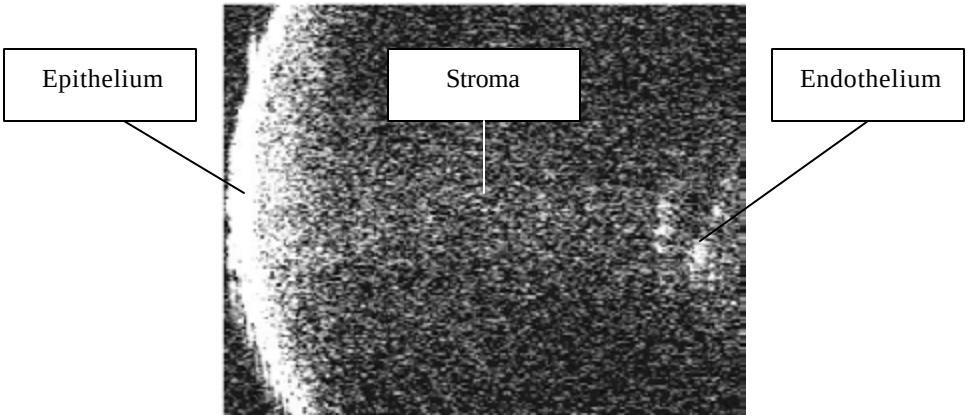

Figure 3.50 Pig cornea detection with SOCT system.

Once the system can acquire information from the cornea, a second cornea is placed onto the mounting and many tests are performed at different pressures simulating different eye conditions. Figure 3.51 shows different phase maps from the cornea at different pressures. Sequences of 200 images are recorded to generate a movie showing changes in time in the cornea. Sequences are taken at different pressures and increments to identify elastic changes on it.

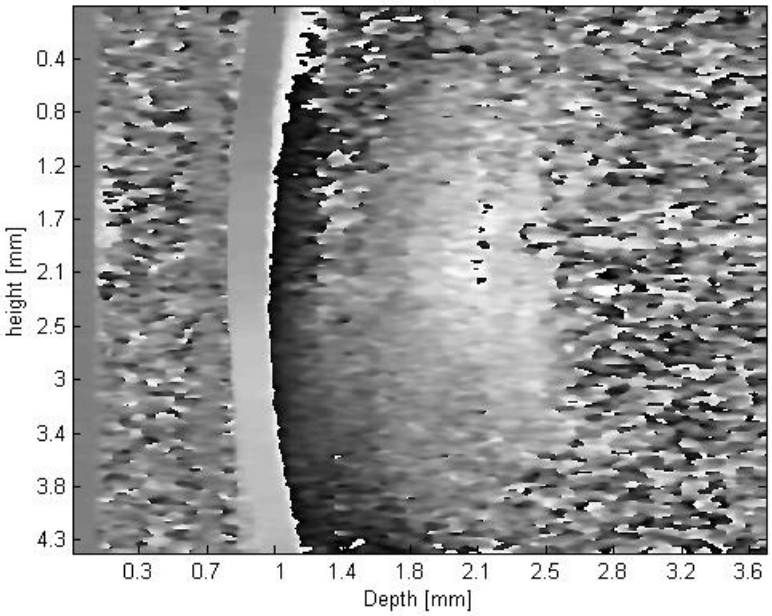
height [mm]
0.4
0.8
1.2
1.7
2.1
2.5
3
3.4
3.8
4.3
0.3
0.7
1
1.4
1.8
2.1
2.5
2.8
3.2
3.6
Depth [mm]

(a)

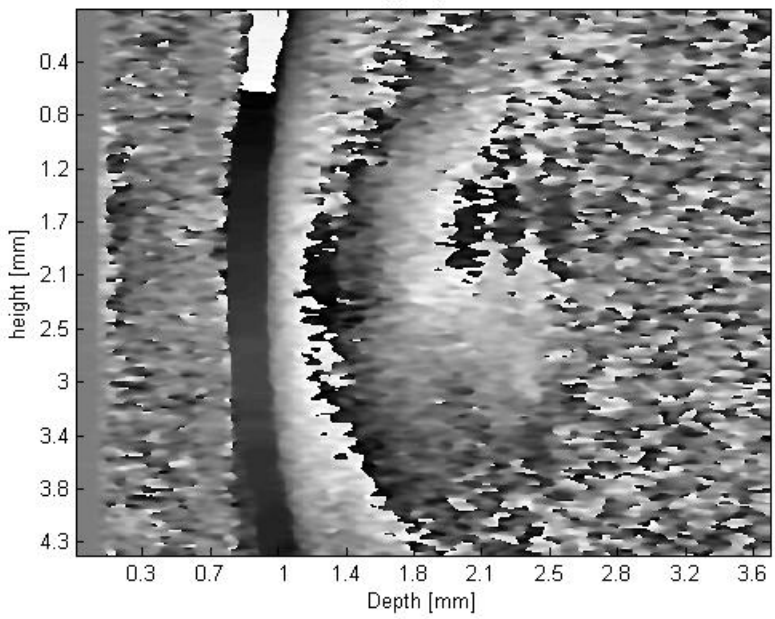
height [mm]
0.4
0.8
1.2
1.7
2.1
2.5
3
3.4
3.8
4.3
0.3
0.7
1
1.4
1.8
2.1
2.5
2.8
3.2
3.6
Depth [mm]

(b)

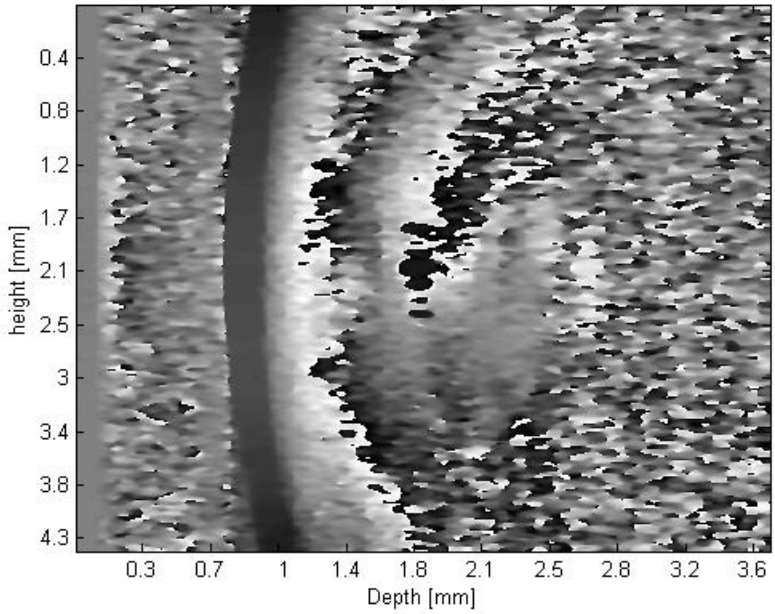

(c)

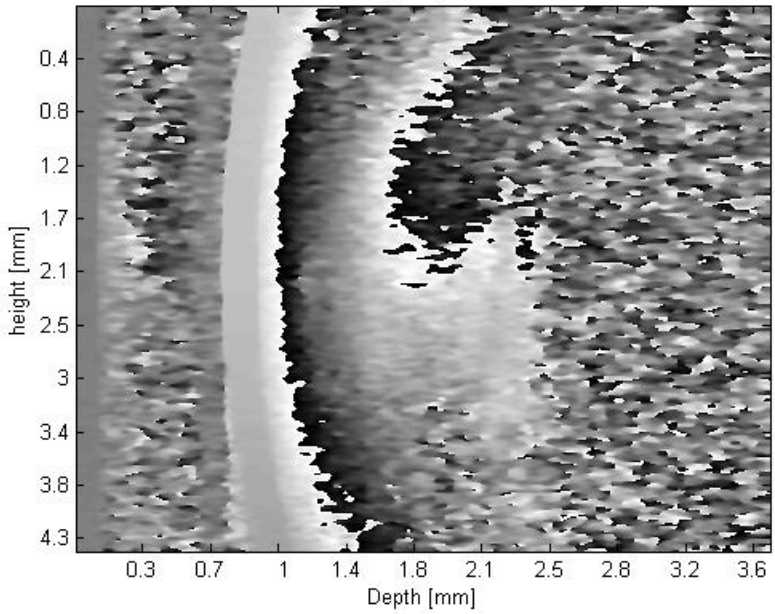

(d)

Figure 3.51 Pig cornea phase maps at (a) 2kP (b) 4kP (c) 6kP (d) 8kP.

Exposure time is ~250 ms.

4. Discussion and conclusions

DHI with three different positions of illumination is a method that can be applied for surface strain detection in metallic objects. The two normal strain gradients give a first approximation for the strain present on the surface of the object. These two gradients have at least mixed information for the x and y variables. The separation of the displacement components allows the isolation of the contributions x and y for each strain gradient. That gives two maps with two variables each one that in turn reduces the information to analyze. By separating each gradient in its two variables it is possible to observe the changes in magnitude that generate the gradients. Results showed a high sensitivity method with high density vector areas. The x dependent gradient maps are from different gradients, having the advantage of different contributions at a time; and likewise for the y dependent gradient maps. Having all this data coming from the DHI method make it possible to move into a new way of processing data. Besides in real applications most of the time samples are not available for long time inspections. So a double exposure time technique has to be reliable enough to get all required information in a very short time with the simplest deformation avoiding any contact with the object.

Finally, considering that both objects were thin aluminum plates the deformations applied modified mostly the x direction (figure 3.16, 3.17, and 3.21 to 3.24). This is observed in the x dependent gradient maps where the strain is more evident. This

condition changes if the object is held in different manners or if the deformation is applied in more than one direction (figure 3.12 to 3.15).

Concerning the use of Spectral Optical Coherence Tomography to measure depth-resolved structure within a sample, this has been extended so as to allow the measurement of depth-resolved displacement fields which is a new interpretation of OCT results. The use of phase information offers displacement sensitivity in the range of a few tens of nm which is a typical good value, some two to three orders of magnitude better than the depth resolution of state-of-the-art OCT systems. The proposed system provides displacement maps within a 2-D slice extending into the sample, and the fact that all the data for a given deformation state are acquired in a single shot is a highly attractive feature for in vivo investigations in the biological sciences. Furthermore, only low cost components are required (the camera used in the experiments described here for example was a CMOS web cam), much larger bandwidths are achievable than with the commonly available tunable light sources needed for wavelength scanning interferometry, and there are no moving parts. Both a theoretical treatment and experimental validation of the concept on a simple well-controlled geometry. The applicability to more complex sample geometries and scattering materials will be investigated. Figures 3.51(a)(b)(c)(d) show relative phase maps from a pig cornea during a hydrostatic test which is a continuous sample. Here it is possible to probe the system response in a real sample. The system used was made

simpler by having a separate reference surface and not a common path configuration [60-62].

Regarding the organic tissues it was possible to detect phase inside this media even when very low back scattering is received back to the system. Figure 3.50 is a good example of this, where stroma region has a very low magnitude. High sensitivity is the biggest advantage in this system able to be used in live samples.

5. References

[1] M. Michalski, H. J. Rabal, and M. J. Garavaglia, "Operations using fringe projection," *Appl. Opt.* **25**, 4338 (1986)

[2] S. Wang, C. J. Tay, C. Quan, and H. M. Shang, "Investigation of Membrane Deformation by a Fringe Projection Method," *Appl. Opt*. **41**, 101 (2002)

[3] N. Takai and T. Asakura, "Displacement measurement of speckles using a 2-D level-crossing technique," *Appl. Opt*. **22**, 3514 (1983)

[4] J. S. Kim, "Range and accuracy of speckle displacement measurement in double-exposure speckle photography," *J. Opt. Soc. Am. A* **6**, 675 (1989)

[5] R. S. Sirohi and N. K. Mohan, "In-plane displacement measurement configuration with twofold sensitivity," *Appl. Opt*. **32**, 6387 (1993)

[6] D. J. Chen, F. -P. Chiang, Y. S. Tan, and H. S. Don, "Digital speckle-displacement measurement using a complex spectrum method," *Appl. Opt*. **32**, 1839 (1993)

[7] D. E. Duffy, "Moire gauging of in-plane displacement using double aperture imaging," *Appl. Opt*. **11**, 1778 (1972)

[8] M. L. Basehore and D. Post, "Displacement fields (U,W) obtained simultaneously by moire interferometry," *Appl. Opt*. **21**, 2558 (1982)

[9] W. Wang and J. Sun, "A modified moire interferometer for three-dimensional displacement measurement," *Chin. Opt. Lett*. **2**, 396 (2004)

[10] Vladimir S. Pisarev, et al. *Strain and Stress Analysis by Holographic and Speckle*, John Wiley & Sons Ltd (1996)

[11] F. Mendoza Santoyo, G. Pedrini, S. Schendin, and H. J. Tiziani, "3D displacement measurements of vibrating objects with multi-pulse digital holography", *Meas. Sci. Tech.* **10**, 1305 (1999)

[12] R. D. Flack, J. G. Thacker, and J. G. Dixon, "Moire interferometry strain measurements in elastic thin membranes," *App. Opt.* **18** 3841 (1979)

[13] Chiang, F. P. and A. Asundi, "Interior Displacement and Strain-Measurement Using White-Light Speckles." *App. Opt*. **19** 2256 (1980)

[14] Chiang, F. P. and C. C. Kin, "Displacement and Strain-Measurement on Curved Surfaces Using Objective Laser Speckles." *JOSA* **71** 1586 (1981)

[15] Chiang, F. P. and D. W. Li, "Random (Speckle) Patterns for Displacement and Strain-Measurement - Some Recent Advances." *Opt. Eng.* **24** 936 (1985)

[16] Feiel, R. and P. Wilksch, "High-resolution laser speckle correlation for displacement and strain measurement." *App. Opt.* **39** 54 (2000)

[17] Reinhard Feiel and Philip Wilksch, "High-resolution laser speckle correlation for displacement and strain measurement", *App. Opt.* **39** 54 (2000)

[18] Michael Spajer, Pramod K. Rastogi, Jacques Monneret, "In-plane displacement and strain measurement by speckle interferometry and moiré derivation", *App. Opt.* **20** 3392 (1981)

[19] Albert S. Kobayashi, *Handbook on experimental mechanics*, VCH-SEM, first edition, (1993)

[20] James W. Dally, William F. Riley, *Experimental stress analysis*, Mc Graw Hill, third edition (1991)

[21] Richard W. Hertzberg, *Deformation and fracture mechanics of engineering materials*, John Wiley & Sons Inc., (1996)

[22] Akhtar S. Khan, Xinwei Wang, *Strain measurements and stress analysis*, Prentice Hall, first edition (2001)

[23] Gary Cloud, *Optical methods of engineering analysis*, Cambridge University Press, first edition (1995)

[24] James F. Shackelford, William Alexander, *Materials science and engineering handbook*, CRC Press, third edition, (2001)

[25] Roy R. Graig Jr., *Mechanics of materials*, John Wiley & Sons, first edition (1996)

[26] Raymond J. Roark and Warren C. Young, *Formulas for stress and strain*, Mc Graw Hill, fifth edition, (1982)

[27] E.J. Hearn, *Mechanics of materials*, Butterworth Heinemann, second edition, (1996)

[28] W. Schumann – m. Dubas, *Holographic Interferometry*, Springer, (1979)

[29] Schumann - Zürcher - Cuche, *Holography and deformation analysis*, Springer, (1985)

[30] Svein Winther, "3D strain measurements using ESPI", *Opt. Las. Eng.* **8**, 45 (1988)

[31] R. Jones, C. Wykes, *Holographic and Speckle Interferometry*, Cambridge Studies in Modern Optics, second edition (1989)

[32] Kjell J. Gåsvik, *Optical metrology*, John Wiley & Sons, third edition (2002)

[33] Manuel De la Torre, et al., "Detection of surface strain by three-dimensional digital holography", *App. Opt.* **44**, 27 (2005)

[34] Manuel De la Torre, et al., "Surface strain distribution on metallic thin plates using 3D digital holographic interferometry", *Opt. Eng.* accepted for publication (March 2006)

[35] Brett E. Bouma, Guillermo J. Tearney, *Handbook of Optical Coherence Tomography*, Marcel Dekker, (2002)

[36] A. F Fercher, W. Drexler, C. K. Hitzenberger and T. Lasser, "Optical coherence tomography –principles and applications," *Rep. Prog. Phys*. **66** 239 (2003)

[37] P.H. Tomlins and R.K. Wang, "Theory, developments and applications of optical coherence tomography", *J. Phys. D.* **38** 2519 (2005)

[38] Mitsuo Takeda, Hideki Ina, Seiji Kobayashi, "Fourier-transform method of fringe-pattern analysis for computer-based topography and interferometry", *JOSA*, **72**, 156 (1982)

[39] F. Mendoza Santoyo, D. Kerr y J.R. Tyrer, "Manipulation of the Fourier components of speckle fringe patterns as part of an interferometric analysis process", *Journal of Modern Optics*, **36**, 195 (1989)

[40] C. K. Hitzenberger, Adolf F. Fercher, "Differential phase contrast in optical coherence tomography," *Opt. Let.* **24**, 622 (1999)

[41] M. A. Choma, et al. "Spectral-domain phase microscopy" *Opt. Let.* **30**, 1162 (2005)

[42] C. Joo, Taner Akkin, Barry Cense, Boris H. Park and Johannes F. de Boer, "Spectral-domain optical coherence phase microscopy for quantitative phase-constrast imaging" *Opt. Let.* **30**, 2131 (2005)

[43] M. Wojtkowski, et al., "In vivo human retinal imaging by Fourier domain optical coherence tomography," *Journal of Biomedical Optics* **7**, 457 (2002)

[44] M. A. Choma, et al., "Sensitivity advantage of swept source and Fourier domain optical coherence tomography," *Opt. Exp.* **11**, 2183 (2003)

[45] J. F. de Boer, et al., "Improved signal-to-noise ratio in spectral-domain compared with time-domain optical coherence tomography," *Opt. Let.* **28**, 2067 (2003).

[46] M. Wojtkowski, et al., "Ultrahigh-resolution, high-speed, Fourier domain optical coherence tomography and methods for dispersion compensation," *Opt. Exp.* **12**, 2404 (2004)

[47] B. Cense, et al., "Ultrahigh-resolution high-speed retinal imaging using spectral-domain optical coherence tomography," *Opt. Exp.* **12**, 2435 (2004)

[48] Y. Yasuno, S. Makita, T. Endo, G. Aoki, H. Sumimura, M. Itoh and T. Yatagai, "One-shot-phase-shifting Fourier domain optical coherence tomography by reference wavefront tilting," *Opt. Exp.* **12**, 6184 (2004)

[49] R. A. Leitgeb, L. Schmetterer, C. K. Hitzenberger, A. F. Fercher, F. Berisha, M. Wojtkowski and T. Bajraszewski, "Real-time measurement of in vitro flow by Fourier-domain color Doppler optical coherence tomography," *Opt. Let.* **29**, 171 (2004)

[50] B. H. Park, M. C. Pierce, B. Cense, S. H. Yun, M. Mujat, G. J. Tearney, B. E. Bouma and J. F. de Boer, "Real-time fiber-based multi-functional spectral domain optical coherence tomography at 1.3μm," *Opt. Exp.* **13**, 3931 (2005)

[51] B. H. Park, et al., "Optic axis determination accuracy for fiber-based polarization-sensitive optical coherence tomography," *Opt. Let.*, **30**, 2587 (2005)

[52] R. Leitgeb, C. K. Hitzenberger and A. F. Fercher, "Performance of Fourier domain vs. time domain optical coherence tomography," *Opt. Exp.* **11**, 889 (2003)

[53] P. D. Ruiz, Y. Zhou, J. M. Huntley and R. D. Wildman, "Depth-resolved whole field displacement measurement using wavelength scanning interferometry," *J. Opt. A: Pure App. Opt.* **6**, 679 (2004)

[54] P. D. Ruiz, J. M. Huntley and R. D. Wildman, "Depth-resolved whole-field displacement measurements by wavelength-scanning electronic speckle pattern interferometry," *App. Opt.* **44**, 3945 (2005)

[55] A. F. Zuluaga and R. Richards-Kortum, "Spatially resolved spectral interferometry for determination of subsurface structure," *Opt. Let.* **24**, 519-521 (1999)

[56] Staffan Schedin, Giancarlo Pedrini, Hans J. Tiziani, Fernando Mendoza Santoyo, "Simultaneous three-dimensional dynamic deformation measurements with pulsed digital holography", *App. Opt.* **38**, 7056 (1999)

[57] Y. Teramura, M. Suekuni and F. Kannari, "Two-dimensional optical coherence tomography using spectral domain interferometry," Journal of Optics A: Pure Appl. Opt. 2, 21-26 (2000).

[58] Kevin Anderson, et. al., "Aplication of structural analysis to the mechanical behaviour of the cornea," *J. Royal Soc.* **1**, 1 (2004)

[59] Yanjun Zeng, et. al, "A comparison of biomechanical properties between human and porcine cornea," *J. Biomech.* **34**, 533 (2001)

[60] Hauger, C., M. Worz, et al. "Interferometer for optical coherence tomography" *App. Opt.* **42** 3896 (2003)

[61] Rollins, A. M. and J. A. Izatt "Optimal interferometer designs for optical coherence tomography" *Opt. Let.* **24** 1484 (1999)

[62] Vakhtin, A. B., D. J. Kane, et al. "Common-path interferometer for frequency-domain optical coherence tomography" *App. Opt.* **42** 6953 (2003)

Appendix A: Sensitivity vector

The speckle random phase distribution is high sensitive to any change present on the object (such displacement or rotation). Considering figure A.1,

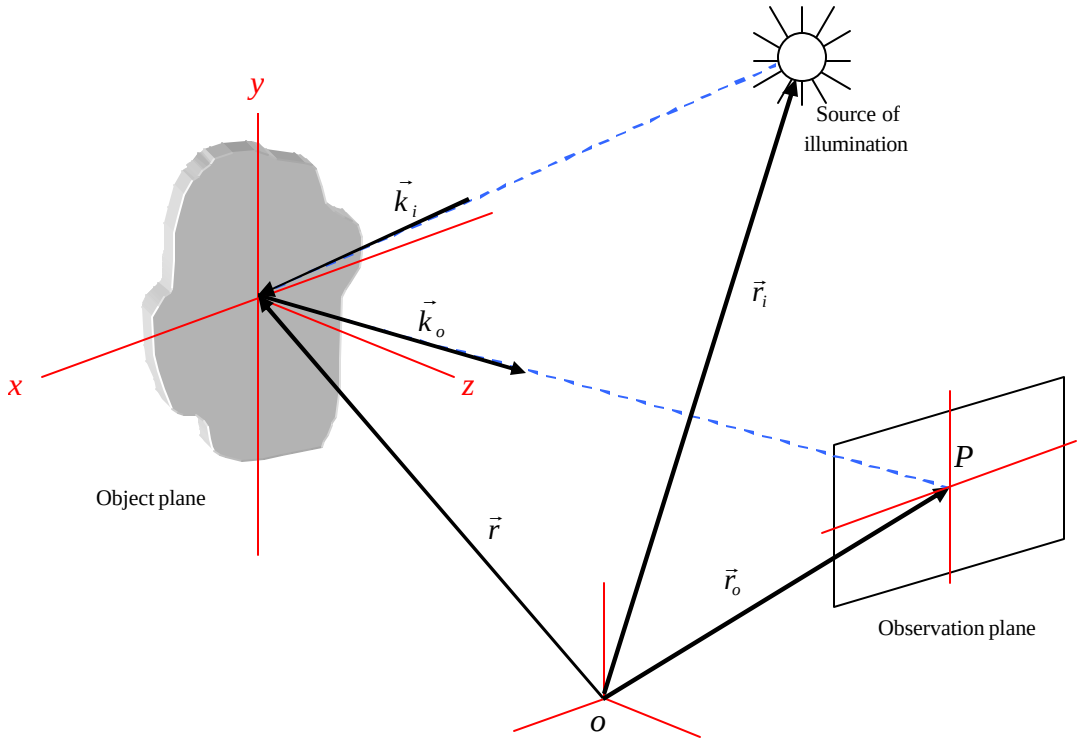

Figure A.1 Schematic geometry to study the sensitivity vector.

the observed speckle phase pattern in a point (P) on the observation plane can be expressed as function of the distance between the source of illumination and the point of observation (P), as follows,

$$y = y_p + f = y_p + f_i + \vec{k}_i(r - r_i) + \vec{k}_o(r_o - r) \qquad \text{A.1}$$

The speckle total phase term can be considered as the sum of two components, the first one is a random component (y_p) and the second one is a deterministic factor (f) which

is integrated with an initial phase coming from the source of illumination (f_i) and successive changes during the light propagation from the source $\vec{k}_i(r - r_i)$ until the observation point $\vec{k}_o(r_o - r)$. These two last phase changes are determined with the object position vector (r), the source position vector (r_i) and the observation position vector (r_o). Defining the illumination and the observation vectors as function of unitary vectors, we have,

$$\vec{k}_i = \frac{2p}{l}\hat{n}_i \qquad \text{A.2}$$

$$\vec{k}_o = \frac{2p}{l}\hat{n}_o \qquad \text{A.3}$$

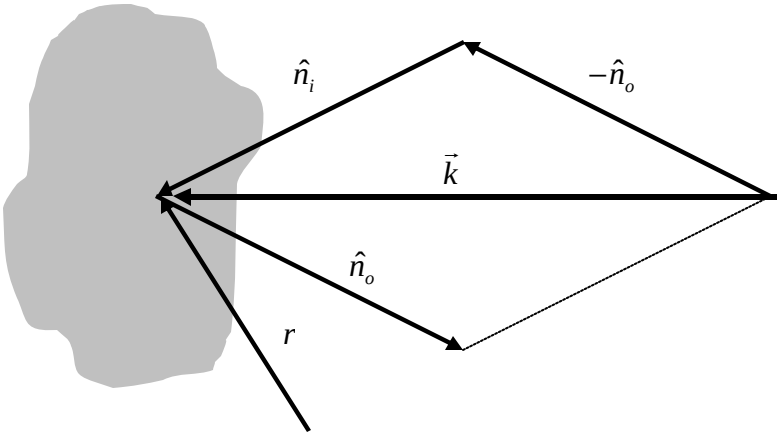

Figure A.2 Sensitivity vector schematic array

From figure A.2 the sensitivity vector k is defined as follows:

$$\vec{k} = \hat{n}_i - \hat{n}_o \qquad \text{A.4}$$

Substituting A.2, A.3 and A.4 in equation A.1:

$$y = y_p + f_i + \frac{2p}{l}\vec{k} \bullet \vec{r} + k_o r_o - k_i r_i \qquad \text{A.5}$$

where changing phase conditions of the object illumination can be expressed as follows,

$$\Delta y = \Delta y_p + \Delta f' + \Delta\left(\frac{2p}{l}\vec{k}\bullet\vec{r}\right)$$

$$\Delta y = \Delta y_p + \Delta f' + \frac{2p}{l}\Delta\vec{k}\bullet\vec{r} + \frac{2p}{l}\Delta\vec{k}\bullet\Delta\vec{r} + \frac{2p}{l}\vec{k}\bullet\Delta\vec{r} \qquad \text{A.6}$$

where $\Delta f'$ is $\Delta f' = f_i + k_o r_o - k_i r_i$. From equation A.6 it is possible to neglect the first term if the displacements applied to the object do not change its micro structure. In a similar way the third term can be annulated if the illumination geometry does not change. The fourth term can be cancelled considering it as the sum of changes in both parameters. Finally, phase sensitivity due the displacement of the object is given as function of the sensitivity vector shown in equation A.7.

$$\Delta y = \frac{2p}{l}\vec{k}\bullet\Delta\vec{r} \qquad \text{A.7}$$

The sensitivity vector can be expressed as matrix form (see equation A.8). In this way sub index i will represents a different illumination direction.

$$\Delta y_i = \frac{2p}{l}\vec{k}_i\bullet\Delta r \qquad i = 1,2,3 \qquad \text{A.8}$$

Considering equation A.8 an illumination distribution is needed in order to have maximization in the sensitivity vector. In section 3.1.1 a sphere section was proposed to have a minimum optical path difference. Considering figure A.3a the three illuminations are situated on this sphere surface. But considering independent relation among them an extended array position is proposed in order to have a contribution at each axis (see figure A.3b).

In figure A.3b each object beam is situated avoiding undesired shadows in the camera. However, sphere area was reduced at ~¼ considering the field of view of the system.

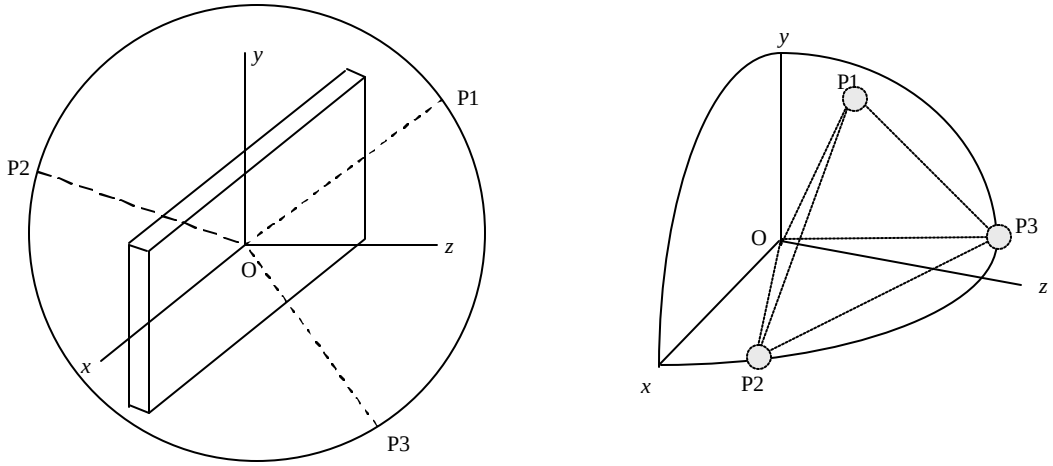

Figure A.3a Proposed sphere of illumination, object centre (O), illumination position 1, 2 and 3 (P1, P2 and P3). A.3b Illumination distribution in the real sphere section observed with the system. Each point of illumination is situated where any axis cancellation occurs.

Appendix B: Strain box design algorithm